



## Electrical Resistivity Dynamics beneath a Fractured Sedimentary Bedrock Riverbed in Response to Temperature and Groundwater/Surface Water Exchange

Colby M. Steelman<sup>1</sup>, Celia S. Kennedy<sup>2</sup>, Donovan Capes<sup>2</sup>, Beth L. Parker<sup>1,2</sup>

<sup>1</sup>School of Engineering, University of Guelph

<sup>2</sup>School of Environmental Sciences, University of Guelph

Correspondence to: Colby M. Steelman ([csteelma@uoguelph.ca](mailto:csteelma@uoguelph.ca))

1 **Abstract.** Bedrock rivers occur where surface water flows along an exposed rock surface. Fractured sedimentary  
2 bedrock can exhibit variable groundwater residence times, anisotropic flow paths, heterogeneity, along with  
3 diffusive exchange between fractures and rock matrix. These properties of the rock will affect thermal transients in  
4 the riverbed and groundwater-surface water exchange. In this study, surface electrical methods were used as a non-  
5 invasive technique to assess the scale and temporal variability of riverbed temperature and groundwater-surface  
6 water exchange beneath a sedimentary bedrock riverbed. Conditions were monitored on a semi-daily to semi-  
7 weekly interval over a full annual period that included a seasonal freeze-thaw cycle. Surface electromagnetic  
8 induction and electrical resistivity imaging methods captured conditions beneath the riverbed along a pool-riffle  
9 sequence within the Eramosa River, Guelph, Ontario, Canada. Geophysical datasets were accompanied by  
10 continuous measurements of aqueous specific conductance, temperature and river stage. Vertical temperature  
11 profiling conducted in an inclined borehole underlying the river revealed active groundwater flow zones through  
12 fracture networks within the upper 10 m of rock. Resistivity measurements during cooler high-flow and warmer  
13 low-flow conditions identified a spatiotemporal riverbed response that was largely dependent upon riverbed  
14 morphology and groundwater temperature. Time-lapse resistivity profiles collected across the pool and riffle  
15 identified seasonal transients within the upper 2 m and 3 m of rock, respectively, with spatial variations controlled  
16 by riverbed morphology (pool versus riffle) and dominant surficial rock properties (competent versus weathered  
17 rock rubble surface). While the pool and riffle both exhibited a dynamic resistivity through seasonal cooling and  
18 warming cycles, conditions beneath the pool were more dynamic, largely due to the formation of river ice.  
19 Although seasonal resistivity trends beneath the riverbed suggest groundwater discharge may be influencing the  
20 spatiotemporal extent of a groundwater-surface water mixing zone, intraseasonal resistivity transience suggest  
21 potential groundwater-surface water exchange across the upper few meters of rock.

22



## 23 1 Introduction

24 Fractured sedimentary bedrock represents an important source of water for many communities around the world.  
25 Although the effective porosity of rock is low relative to unconsolidated sediment, the existence of dense networks  
26 of interconnected fractures, dissolution-enhanced conduits, and karst features, can result in productive yet  
27 heterogeneous and anisotropic flow systems. An exposed bedrock surface may exhibit greater variability in flow  
28 and transport properties as it is subjected to weathering and erosional processes. This can lead to very complicated  
29 groundwater recharge and discharge patterns particularly in areas hosting dynamic interactions between  
30 groundwater and surface water.

31 Fractured rock may be conceptualized as a dual porosity system where fractures dominate flow, but remain  
32 connected to water stored in the porous matrix through advection and diffusion. Such conceptualizations of fracture  
33 flow and transport are routinely applied to groundwater resource (e.g., Novakowski and Lapcevic, 1998; Lemieux et  
34 al., 2009; Perrin et al., 2011) and contaminant transport studies (e.g., Zanini et al., 2000; Meyer et al., 2008;  
35 McLaren et al., 2012). While a number of recent studies have extended some of these concepts to fluvial  
36 depositional environments (e.g., Singha et al., 2008; Toran et al., 2013a), there remain gaps in our conceptual  
37 understanding of groundwater-surface water interaction and exchange mechanisms in bedrock rivers where discrete  
38 fracture networks will dominate groundwater-surface water flux with secondary interactions supported by the porous  
39 rock matrix.

40 Groundwater-surface water interactions at the reach-scale are conceptualized through gaining, losing and flow-  
41 through interactions (Woessner, 2000). At the channel scale, micro-to-macro bedform variations result in variably-  
42 scaled surface water downwelling (recharge) zones and groundwater upwelling (discharge) zones (e.g., Binley et al.,  
43 2013; Käser et al., 2013). Groundwater temperature measurements are routinely used to evaluate spatiotemporal  
44 variations in groundwater-surface water exchange or flux across riverbeds (e.g., Anderson, 2005; Irvine et al., 2016).  
45 Yet, very little is known about the existence and nature of groundwater-surface water mixing zones in fractured  
46 sedimentary bedrock, largely because these systems are very difficult to instrument using direct methods (e.g., drive  
47 point monitoring wells, seepage meters, thermistors) and the scale of the interaction may be very small or  
48 heterogeneous relative to equivalent processes in unconsolidated sediment.

49 Hydrologic processes along a fractured bedrock river were explored by Oxtobee and Novakowski (2002), who  
50 concluded that groundwater-surface water interaction was restricted by poor vertical connectivity and limited  
51 bedrock incision (i.e., exposure of bedding plane fractures). A subsequent numerical sensitivity analysis by Oxtobee  
52 and Novakowski (2003) confirmed that groundwater-surface water connectivity through discrete fractures would be  
53 highly variable in space and time, and would largely depend on fracture size or aperture, river stage, and the  
54 distribution of hydraulic head within the flow system. Fan et al. (2007) numerically explored the influence of  
55 larger-scale fracture orientations and geometries on the groundwater flow system near a stream. Although these  
56 previous studies offered valuable insights into the magnitude of groundwater-surface water exchange, they were  
57 based on idealized fracture network conceptualizations, and did not consider the role of matrix porosity and potential  
58 exchanges between fractures and the porous matrix.



59 Fractured sedimentary bedrock exhibits complex flow systems, where the bulk of the flow occurs in the fracture  
60 network, with highly-variable head distributions; matrix storage may support equally complex biogeochemical  
61 processes and thermal dynamics through convective or diffusive exchange with open fractures or dissolution-  
62 enhanced features (Fig. 1). Ward et al. (2010a) demonstrated how surface electrical methods can be used to detect  
63 and quantify diffusive mass transport (exchange) between a mobile and immobile storage zone in a shallow  
64 riverbed. Therefore, we hypothesize that a groundwater-surface water mixing zone – encompassing fracture and  
65 matrix flow and diffusion – may be identified within a fractured bedrock riverbed by monitoring spatiotemporal  
66 changes groundwater temperature and porewater electrical conductivity using minimally invasive electrical  
67 resistivity methods. The detection of seasonal transients beneath the bedrock riverbed would support future  
68 conceptualizations of groundwater-surface exchange along fractured bedrock rivers.

69 Our study focuses on geoelectrical transients along the Eramosa River in Ontario, Canada. Seasonal variations in  
70 electrical resistivity distribution were measured along two transects intersecting a pool-riffle sequence. Based on  
71 continuous measurements of groundwater and surface water temperature, specific conductance and river stage,  
72 spatiotemporal resistivity dynamics were largely controlled by riverbed morphology in combination with seasonal  
73 changes in water temperature and electrolytic concentration. Over a complete annual cycle, formation of ground  
74 frost and basal ice during the winter season was accompanied by stronger geoelectrical dynamics than intraseasonal  
75 (spring, summer and fall) transience in the flow system. These geoelectrical observations support the existence of a  
76 predominant groundwater discharge zone with limited groundwater-surface water mixing.

## 77 **2 Background**

### 78 **2.1 Geophysical Investigations along Streams and Rivers**

79 Electrical and electromagnetic methods such as ground-penetrating radar, electromagnetic induction and electrical  
80 resistivity imaging are commonly used to characterize fluvial deposits (e.g., Naegeli et al., 1996; Gourry et al., 2003;  
81 Froese et al., 2005; Sambuelli et al., 2007; Rucker et al., 2011; Orlando, 2013; Doro et al., 2013; Crosbie et al.,  
82 2014). The capacity of time-lapse electrical resistivity imaging for conceptualization of groundwater transients in  
83 sediment is also documented in the literature (e.g., Nyquist et al., 2008; Miller et al., 2008; Coscia et al., 2011;  
84 Cardenas and Markowski, 2011; Musgrave and Binley, 2011; Coscia et al., 2012; Dimova et al., 2012; Wallin et al.,  
85 2013). Electrical imaging of natural river systems perturbed by solute tracers has resulted in unprecedented  
86 visualizations of fluid flow (e.g., Ward et al., 2010a, 2010b; Doetsch et al., 2012; Ward et al., 2012; Toran et al.,  
87 2013a; Toran et al., 2013b; Harrington et al., 2014). More recent applications of electrical resistivity in karst  
88 undergoing surface water transients have shown how surface geophysics can unravel complex hydrologic processes  
89 in sedimentary bedrock environments (e.g., Meyerhoff et al., 2012; Meyerhoff et al., 2014; Sirieix et al., 2014),  
90 especially when site conditions limit the use of direct measurement methods.

91 While a variety of geophysical tools and techniques can measure flow and water chemistry in space and time  
92 (Singha et al., 2015), the most appropriate tool and approach will depend on the scale of interest. The vast majority  
93 of geophysical work within shallow river environments has utilized discrete temperature monitoring below the



94 riverbed to assess vertical fluxes (e.g., White et al., 1987; Silliman and Booth, 1993; Evans et al., 1995; Alexander  
95 and Caissie, 2003; Conant, 2004; Anderson, 2005; Hatch et al., 2006; Keery et al., 2007; Schmidt et al. 2007;  
96 Constantz, 2008); these works have focused on processes within alluvial sediments. Recent advancements in  
97 distributed fiber optic cables have improved spatial and temporal resolution of groundwater-surface water  
98 interactions (e.g., Slater et al., 2010; Briggs et al., 2012; Johnson et al., 2012).

99 Groundwater and surface water interaction can be monitored through changes in thermal gradient or electrolytic  
100 concentration (e.g., Norman and Cardenas, 2014), yet the scale and magnitude of these interactions will vary as a  
101 function of riverbed architecture and subsurface hydraulic conditions (Crook et al., 2008; Boano et al., 2008; Ward  
102 et al., 2012; Tinkler and Wohl, 1998) resulting in spatially dynamic exchange. These processes are further  
103 complicated by diel (e.g., Swanson and Cardenas, 2010) and seasonal (e.g., Musgrave and Binley, 2011)  
104 temperature fluctuations across a range of spatial scales, local transients such as precipitation events (e.g.,  
105 Meyerhoff et al., 2012), river stage fluctuations (e.g., Bianchin et al., 2011) and controlled dam releases (e.g.,  
106 Cardenas and Markowski, 2011). Relative to other non-invasive geophysical methods, electrical resistivity methods  
107 are more robust in their ability to provide information about temperature and solute fluctuations beneath actively  
108 flowing surface water bodies (e.g., Nyquist et al., 2008; Cardenas and Markowski, 2011; Ward et al., 2012;  
109 Meyerhoff et al., 2014) particularly in a time-lapse manner. Unlike conventional hydrogeological methods (e.g.,  
110 screened or open coreholes), which may bias conduction in the fractures, surface electrical methods are sensitive to  
111 the bulk electrical conductivity of the formation, making them more suited for detection of processes between the  
112 open fractures/conduits and the porous matrix.

## 113 2.2 Electrical Properties of the Subsurface

114 Electrical resistivity methods are based upon Ohm's Law ( $R = \Delta V/I$ ). In the case of a homogeneous half-space,  
115 the electrical resistance ( $R$ ) of the subsurface is determined by measuring the potential difference ( $\Delta V$ ) across a pair  
116 of 'potential' electrodes due to an applied current ( $I$ ) across a pair of 'current' electrodes some distance away. The  
117 measured  $R$  ( $\Omega$ ) across a unit volume of the earth can be converted to apparent resistivity ( $\Omega$  m) using a specific  
118 geometric factor that compensates for varying electrode array geometry (Reynolds, 2012). Apparent resistivity  
119 measurements are commonly interpreted using tomographic inversion techniques, whereby measured data is  
120 reconstructed from forward models of an optimized physical parameter distribution (Snieder and Trampert, 1999;  
121 Loke et al., 2013). Although data inversion techniques are standard practice in the interpretation of most  
122 geophysical data, the model that best matches the measured data is not necessarily an exact representation of the  
123 subsurface. The inversion process ultimately yields a smoothed representation of the actual parameter distribution.

124 The bulk electrical resistivity (i.e., inverse of conductivity) of a formation can be calculated through a simple  
125 empirical relationship known as Archie's Law (Archie, 1942):

$$126 \quad \rho_b = \phi^{-m} \rho_w, \quad (1)$$

127 where the resistivity of the bulk formation ( $\rho_b$ ) is simply related to the porosity of the medium ( $\phi$ ) raised to the  
128 negative power ( $m$ ), which represents the degree of pore cementation, and the resistivity of the pore fluid ( $\rho_w$ )



129 (Glover 2010). This relationship carries a number of simplifying assumptions: the most significant being that the  
130 current flow is entirely electrolytic. While more sophisticated formulations of Archie's Law incorporating fluid  
131 saturation and interfacial conduction can be found in the literature (e.g., Rhoades et al., 1976; Waxman and Smits,  
132 1968), Eq. (1) is considered to be a reasonable approximation in a saturated relatively clay-free environment.  
133 Equation (1) is used in this study to evaluate the impact of observed groundwater and surface water aqueous  
134 conductivity variations on the bulk formation resistivity. Here, a value of 1.4 was used for the constant  $m$ , which is  
135 considered reasonable for fractured dolostone. It should be noted that the relative impact of aqueous conductivity  
136 changes on the bulk formation resistivity may vary with clay content and pore connectivity due to intrinsic  
137 deviations in the  $m$  value (Worthington, 1993). Furthermore, orientated fracture networks may result in an  
138 anisotropic resistivity response (Steelman et al., 2015b); however, these static properties of the rock will not impact  
139 relative changes in resistivity at a fixed location.

140 The electrolytic (fluid phase) resistivity will depend on the concentration and composition of dissolved ions, and  
141 viscosity of the pore water (Knight and Endres, 2005). Increasing ion concentrations and temperature will lead to a  
142 reduction in formation resistivity. Empirical evidence has shown that resistivity can decrease anywhere from 1 % to  
143 2.5 % per °C (Campbell et al., 1948; Keller, 1989; Brassington, 1998). Temperature corrections can be made using  
144 Arp's law (Arps, 1953):

$$145 \rho_{w2} = \frac{\rho_{w1}(T_1 + 21.5)}{(T_2 + 21.5)}, \quad (2)$$

146 where  $\rho_w$  ( $\Omega$  m) and  $T$  (°C) represent the resistivity and temperature of the water at two points. This formulation  
147 was developed from a least-squares fit to the conductivity of a NaCl solution ranging from 0°C to 156°C; however,  
148 the exact relationship between fluid conductivity and temperature will depend on the composition of the electrolytic  
149 solution (Ellis, 1987).

### 150 2.3 Field Site Description

151 The Eramosa River is a major tributary of the Speed River within the Grand River Watershed, Ontario, Canada, and  
152 resides upon a bedrock aquifer of densely fractured dolostone of Silurian age with dissolution-enhanced conduits  
153 and karst features (e.g., Kunert et al., 1998; Kunert and Coniglio, 2002; Cole et al., 2009). Outcrops, core logs and  
154 geophysical data collected along the Eramosa River (e.g., Steelman et al., 2015a; Steelman et al., 2015b) indicate  
155 abundant vertical and horizontal fracture networks and karst features intersecting and underling the river. These  
156 field observations support the existence of a potential groundwater-surface water mixing controlled by discrete  
157 fracture networks and dissolution-enhanced features.

158 A focused geophysical investigation was carried out along a 200 m reach of the Eramosa River (Fig. 2). The study  
159 area was positioned at a bend in the river with relatively cleared vegetation along the south shoreline and adjacent  
160 floodplain with exposed rock at surface. A network of coreholes (continuously cored boreholes) and streambed  
161 piezometers were installed across the site. Locally, the water table elevation corresponds to the surface water or  
162 stage elevation, resulting in vadose zone thicknesses between <0.5 m to 2.0 m along the shorelines. The temperate



163 southern Ontario climate subjects the river to a wide-range of seasonal conditions, including high precipitation  
164 periods in spring and fall, hot and dry summers, and variable degrees of ground frost and surface water freeze-up  
165 during the winter months (Fig. 3a).

166 Locally, the river incises the Eramosa Formation by 2 m to 3 m exposing abundant vertical and horizontal fractures  
167 with little to no alluvial sediment deposited along the riverbed (Fig. 3b). Regionally the Eramosa acts as a  
168 discontinuous aquitard unit (Cole et al. 2009); however, core logs collected at the study site show bedding plane and  
169 vertical joint set fractures spanning the entire 11 m sequence of Eramosa. This upper formation is underlain by  
170 approximately 3 m of cherty, marble-like Goat Island formation, which exhibits high-angle fractures along cherty  
171 nodules near the Eramosa contact. The Goat Island is underlain by more than 15 m of Gasport, which exhibits coral  
172 reef mounds of variable morphology. The rock matrix of the Gasport is visually more porous with well-defined  
173 vugs, dissolution-enhanced features, and fewer fractures than the overlying Goat Island and Eramosa. A full-  
174 description of these bedrock sequences can be found in Brunton (2009).

175 In this region, the winter season may be accompanied by ground frost formation and variable surface water freezing.  
176 Seasonal freeze-up will consist of an ice crust layer on the surface of the water and the possible formation of basal  
177 ice along the riverbed (Stickler and Alfredsen, 2009). This phenomenon can occur during extreme atmospheric  
178 cooling over turbulent water bodies, resulting in super-cooled water ( $<0^{\circ}\text{C}$ ) that rapidly crystallizes to form frazil  
179 (i.e., tiny ice particles with adhesive characteristics); these crystals can flocculate to form slush, which adheres and  
180 accumulates on the substrate forming a basal ice layer.

### 181 **3 Methods**

#### 182 **3.1 Bedrock Lithology, Fractures and Porosity**

183 The geology was characterized through a series of vertical and angled coreholes along the southern shoreline that  
184 were advanced into upper Gasport formation. These drilling activities were part of a broader hydrogeological  
185 investigation of groundwater flow and fluxes along the river. A network of riverbed piezometers, bedrock stage  
186 gauges, and flux measurement devices were installed between 2013 and 2014 within the pool. Locally, the riverbed  
187 morphology can be distinguished in terms of the amount of bedrock rubble or weathered rock fragments blanketing  
188 the exposed rock surface. Figure 2 shows the transition from a rubble dominated riverbed (RDR) to a more  
189 competent rock riverbed (CRR); this boundary roughly corresponds to the riffle-pool transition.

190 Geophysical measurements were supported by temperature, specific conductance of the fluid and river stage  
191 elevation collected at nearby monitoring points (Fig. 2). The geologic and hydrogeologic data were obtained from a  
192 river stage gauge (RSG4), a vertical corehole (SCV6) drilled to a depth of 10.9 m, and an angled corehole (SCA1)  
193 drilled to a vertical depth of 31.8 m. The angled corehole plunges at  $60^{\circ}$  and is orientated at  $340^{\circ}$ , and therefore,  
194 plunges beneath the river with a lateral footprint spanning approximately 21 m from its surface expression.  
195 Coreholes were drilled using a small-diameter portable Hydrocore Prospector™ drill with a diamond bit (NQ size:  
196 47.6 mm core and 75.7 mm corehole diameter) and completed with steel casings set into concrete to a depth of 0.6



197 m below ground surface (bgs). All coreholes were sealed using a flexible impermeable liner filled with river water  
198 (FLUTE™ Flexible Liner Underground Technologies, Alcalde, New Mexico, USA) (Keller et al., 2014).

199 The SCA1 rock core was logged for changes in lithology, vugs, and fracture characteristics, intensity and  
200 orientation, including bedding plane partings. Rock core subsamples were extracted for laboratory measurements of  
201 matrix porosity using the following procedure: sample was oven dried at 40°C; dimensions and dry mass recorded;  
202 samples evacuated in a sealed chamber and imbibed with deionized water; sample chamber pressurized to 200 psi to  
203 300 psi for 15 minutes; samples blotted and weighed to obtain saturated mass. Open coreholes were logged using an  
204 acoustic (QL40-ABI) and an optical (QL40-OBI) borehole imager (Advanced Logic Technologies, Redange,  
205 Luxembourg), to characterize the fracture network.

### 206 **3.2 Pressure, Temperature, Specific Conductance and River Flux**

207 Temperature, specific conductance and hydraulic pressure data were recorded using a CTD-Diver™ (Van Essen  
208 Instruments, Kitchener, Canada) deployed within RSG4 (surface water) and SCV6 (groundwater) at a depth of 10.5  
209 m bgs. The transducer in SCV6 was placed near the bottom of the open corehole prior to being sealed with an  
210 impermeable liner, thereby creating a depth-discrete groundwater monitoring point. Surface water data were  
211 recorded through the full study period while deeper bedrock conditions were recorded from early-September 2014  
212 through late-May 2015. All measurements were collected at 15 minute intervals.

213 Vertical temperature profiles were additionally collected along the inclined sealed corehole water column of SCA1  
214 from 4-Sep-2014 to 22-May-2015 using an RBR*solo*™ temperature logger paired with a RBR*solo*™ pressure logger  
215 (RBR Limited, Ottawa, Canada). These data were recorded at 0.5 second intervals while the sensors were manually  
216 lowered into the water column using a fiberglass measuring tape at a rate of 0.02 m s<sup>-1</sup> to 0.03 m s<sup>-1</sup>. Barometric  
217 pressure was collected at the site using a Baro-Diver™ (Van Essen Instruments, Kitchener, Canada).

218 Rainfall was recorded at the University of Guelph Turfgrass Institute, located 2 km northwest of the site, while  
219 snowfall accumulation was obtained from the Region of Waterloo Airport roughly 18 km south west of the site.  
220 Hourly mean river flux was recorded 900 m upstream at the Watson Road gauge operated by the Grand River  
221 Conservation Authority. A summary of the weather and river flux data are provided in Fig. 4.

### 222 **3.3 Riverbed Electrical Resistivity**

#### 223 **3.3.1 Spatial Electrical Resistivity Mapping**

224 Riverbed electrical resistivity distribution was initially measured using a Geonics EM-31 ground conductivity meter  
225 (Geonics, Mississauga, Canada) during a seasonally cool and warm period: early-spring/high-stage conditions on 3-  
226 Apr-2013 and mid-summer/low-stage conditions on 7-Jul-2014. Measurements were collected at a rate of 3  
227 readings per second with the device operated in vertical dipole mode held ~1 m above the riverbed. The effective  
228 sensing depth of this instrument in vertical dipole mode is approximately 6 m, and is minimally sensitive to  
229 conditions above the ground surface (McNeil, 1980). Data was recorded along roughly parallel lines spaced ~1.75  
230 m apart orthogonal to the river orientation, with the coils aligned parallel to surface water flow direction. Water



231 depths over the investigated reach varied from  $<0.1$  m in the riffle during low-flow to nearly 1 m in the pool during  
232 high-flow conditions. Data sets were filtered for anomalous outliers prior to minimum curvature gridding.

### 233 3.3.2 Time-Lapse Electrical Resistivity Imaging

234 Surface electrical resistivity measurements were collected along two transects orientated orthogonal to the river (Fig.  
235 2), capturing conditions within a pool and riffle sequence (Fig. 3). Line 1 was positioned downstream over a deeper  
236 pool section with more substantial bedrock incision into a competent bedrock surface (Fig. 3b, i and ii), while line 2  
237 was situated upstream over a shallower riffle section blanketed by bedrock rubble fragments with less bedrock  
238 incision (Fig. 3b, iii).

239 For this study, resistivity cables were constructed using a pair of 25 multicore cables (22 gauge strained wire, 600V  
240 rating) wound within a PVC jacket. The PVC jacket was split open every meter to expose and cut out a single wire  
241 that was connected to an audio-style banana plug. Spliced sections of outer PVC jacket were resealed using heat  
242 shrink tubing and silicon. This process resulted in two 24 channel cables each connected to a single multi-pin  
243 connector for direct data logger communication. Electrodes were constructed from half-inch diameter stainless steel  
244 rod cut to 6 inch lengths. A hole was drilled on one end of the electrode to receive the banana plug connector.  
245 Given the exposed bedrock across the site, a half-inch hole was drilled into the rock at 1 m intervals along the  
246 ground surface. In some cases, electrodes were buried beneath a rubble zone of the riverbed, or were pushed into a  
247 thin layer of sediment. On the shorelines electrodes were fully implanted into the rock along with a few teaspoons  
248 of bentonite clay to minimize contact resistance. Each monitoring line was instrumented with dedicated electrodes  
249 and cables that remained in place for the duration of the study.

250 Resistivity measurements were recorded using a Syscal Junior Switch 48 (Iris Instruments, Orléans, France)  
251 resistivity meter. A Wenner array was selected for its higher S/N ratio. A dipole-dipole array was tested, but found  
252 to be very susceptible to noise (i.e., excessive number of bad data points due to low measured potentials); this was  
253 attributed to the high-contact resistances with rock combined with the instruments moderate power capability (max  
254 400 V, 1.3 A). Although the Wenner array geometry results in a stronger signal (i.e., potentials are measured across  
255 a pair of electrodes located between the current electrodes with an equal inter-electrode spacing), it will be less  
256 sensitive to lateral variations across the riverbed compared to the dipole-dipole array, and thus, less sensitive to the  
257 presence of a single or package of vertical fractures between adjacent electrodes. Surface resistivity data were  
258 recorded on a semi-daily to semi-weekly interval from 18-Jul-2014 to 3-Jul-2015 covering a complete annual cycle,  
259 which included a seasonal freeze-thaw cycle, and numerous wetting-drying events accompanied by large river stage  
260 fluctuations. The timing of resistivity measurement events are shown with corresponding river flow rates and  
261 atmospheric data in Fig. 4. Resistivity measurements were generally recorded between 8 AM and 1 PM.

262 Measured apparent resistivity data was manually filtered to remove erroneous data points prior to being inverted  
263 using RES2DINV v.3.59 (Geotomo Software, Malaysia), which uses the Gauss-Newton least-squares method (Loke  
264 and Dahlin, 2002). For this study, a robust inversion scheme was used with moderate to high dampening factors  
265 given the high resistivity contrast observed along the surface, and intermittently noisy datasets. The width of the



266 model cells were set to half the electrode spacing (i.e., model refinement) to help suppress the effects of large surface  
 267 resistivity variations on the inversion process. All other parameters within the program were optimized to  
 268 compensate for high noise and large resistivity contrasts while achieving the lowest possible model root mean  
 269 squared (RMS) error.

270 Figure 5 shows the model setup for the pool and riffle, including the minimum and maximum river stage elevations  
 271 observed during the geophysical monitoring events. A portion of the electrodes were variably submerged beneath a  
 272 surface water layer. Stage elevations ranged from 310.92 masl to 311.32 masl at line 1, and 311.09 masl to 311.48  
 273 masl at line 2. Thus, each model was independently inverted with a defined surface water boundary (i.e., stage  
 274 height above the submerged electrodes) and true aqueous resistivity, both of which were fixed for each model  
 275 inversion. Model convergence typically occurred within 8 iterations.

276 Temporal variations in bedrock resistivity were assessed within four representative zones (A, B, C and D; Fig. 5)  
 277 using a resistivity index (*RI*). These zones were chosen based on their contrasting bedrock conditions, relative  
 278 position along the river transect and geophysical dynamics observed during the monitoring period. The *RI* was  
 279 calculated for the pool and riffle resistivity profile as follows:

$$280 \quad RI_{i,j} = \frac{MZR_{i,j} - MAR}{MAR}, \quad (3)$$

281 where  $RI_{i,j}$  = resistivity index for the  $i^{\text{th}}$  zone on the  $j^{\text{th}}$  sample date;  $MZR_{i,j}$  = mean zone resistivity for the  $i^{\text{th}}$  zone  
 282 on the  $j^{\text{th}}$  sample date;  $MAR$  = mean annual resistivity of the entire profile across the full time series for the pool or  
 283 riffle.

## 284 4 Results

### 285 4.1 Bedrock Fracture Network, Temperature and Specific Conductance

286 Formation contacts of the Eramosa–Goat Island and the Goat Island–Gasport formations were identified in core at  
 287 depths of 8.6 and 13.0 m bgs, respectively (Fig. 6a). Fractures beneath the river were predominantly horizontal to  
 288 slightly dipping ( $<10^\circ$ ), and most abundant in the Eramosa and Goat Island. Although vertical and sub-vertical  
 289 fractures ( $>10^\circ$ ) were relatively less abundant, they were more uniformly distributed with depth. These high-angle  
 290 fractures terminate at surface as vertical joint sets along two regional orientations:  $10^\circ$  to  $20^\circ$  NNE and  $280^\circ$  to  $290^\circ$   
 291 SNW (Fig. 3b, ii). Matrix porosities from the corehole were relatively low, ranging from 0.5 % to 5 %, with the  
 292 lowest porosities observed along the highly weathered riverbed surface and lower portion of the Eramosa Formation.  
 293 Hydraulic head data collected in the river and at the base of SCV6 (10.5 m bgs) suggest a seasonally sustained  
 294 upward vertical gradient (i.e., groundwater discharge zone) at the pool.

295 Vertical temperature profiling within the static water column of the FLUTE™ lined SCA1 corehole from 4-Sep-  
 296 2014 to 22-May-2015 captured seasonal fluctuations in ambient groundwater temperature to depths up to 20 m (Fig.  
 297 6b), thereby delineating the vertical extent of the heterothermic zone. Temperatures inside the liner ranged from



298 18°C in late-summer, to 5°C in mid-winter. Although fluctuations were observed along the entire 20 m profile, the  
299 bulk of the variations (short and long-period) were observed in the upper 10 m bgs.

300 Previous studies using ambient temperature profiling in lined coreholes (Pehme et al. 2010; Pehme et al. 2014)  
301 examined the effects of active groundwater flow around static water columns. Pehme et al. (2010) demonstrated  
302 how a lined water-filled corehole in thermal disequilibrium with the surrounding formation would exhibit more  
303 short-period temperature perturbations along its vertical profile than an equilibrated water column within zones of  
304 active groundwater flow. Here, the onset of winter seasonal conditions (9-Jan-2015 through 31-Mar-2015) cooled  
305 the corehole water column near the ground surface resulting in density-driven convection within the column, leading  
306 to thermal disequilibrium with respect to the surrounding bedrock resulting in abrupt temperature perturbations as  
307 the water column cooled toward 5°C. The magnitude and frequency of the perturbations observed in Fig. 6b during  
308 these cooler periods correspond to areas of increased fracture frequency (Fig. 6a), indicating active groundwater  
309 flow zones beneath the riverbed.

310 Specific conductance and temperature of surface water (RSG4) and groundwater (SCV6) corresponding to  
311 geophysical sampling events (Fig. 4) are presented in Fig. 7. These data indicate that surface water specific  
312 conductivity varied within a much narrower range than the actual (uncompensated) conductivity, which includes the  
313 effects of temperature. While the overall impact of temperature and ionic concentration on the specific conductance  
314 of surface water were similar (i.e., equivalently dynamic), variations associated with ionic concentration appear  
315 more erratic, and exhibited sharper fluctuations over shorter periods of time. For instance, major precipitation  
316 events coinciding with measurement events 13, 26 and 31 (refer to Fig.4) were accompanied by short-period  
317 reductions in surface water conductivity and increases in temperature. Seasonal atmospheric temperature trends  
318 resulted in more gradual, yet seasonally sustained reductions in aqueous conductivity. In comparison, the  
319 groundwater specific conductance at 10.5 m bgs was comparatively stable during the study period, exhibiting a  
320 moderate temperature driven decline superimposed by shorter-period fluctuations associated with ion concentration.

321 Figure 8 shows the potential impact of these observed specific conductivity and temperature variations (based on  
322 Fig. 6b and 7) on the bulk formation resistivity using Eq. (1) and Eq. (2) for three representative porosity values.  
323 Porosities of 1 % and 5 % correspond to the values obtained in core, while a porosity of 35 % might represent the  
324 maximum porosity of a weathered or broken rubble zone. These calculations indicate that variations in temperature  
325 will likely be the primary driver in formation resistivity dynamics. For instance, water temperature could affect the  
326 formation resistivity by as much as 46 %, based on the observed range in groundwater and surface water  
327 temperatures, respectively. In comparison, measured aqueous conductivity ranges (along a particular isotherm) for  
328 groundwater and surface water would affect the formation resistivity by 18 % and 36 %, respectively. These  
329 maximum effects represent end-member conditions for a specific porosity. The natural system will exhibit a much  
330 more complex distribution of formation resistivity given variable fracture networks, matrix porosity, and  
331 dissolution-enhanced features.

#### 332 4.2 Sub-Riverbed Electrical Resistivity Distribution



333 Two ground conductivity surveys were conducted across the riverbed to assess spatial variability in bulk formation  
334 resistivity and its relationship to riverbed morphology (e.g., pool vs. riffle): the first resistivity snapshot was  
335 collected on 3-Apr-2013 during high-flow conditions ( $6.81 \text{ m}^3 \text{ s}^{-1}$ ) (Fig. 9a) while the second was collected on 7-Jul-  
336 2014 during low-flow conditions ( $1.30 \text{ m}^3 \text{ s}^{-1}$ ) (Fig. 9b). The daily average river flows for the years 2013 and 2014  
337 were  $3.5 \text{ m}^3 \text{ s}^{-1}$  and  $3.3 \text{ m}^3 \text{ s}^{-1}$ , respectively.

338 Two main observations can be made from the changes observed between cooler high-flow and warmer low-flow  
339 conditions. First, the southern shoreline exhibited the highest resistivity (red areas) with the least temporal  
340 variability. These areas are characterized by more competent and less-fractured rock (Fig. 3b, i). Secondly, a more  
341 dynamic response was observed northward into the thalweg and along the north shoreline; the rock surface in these  
342 areas was more weathered with large irregular rock fragments and dissolution features. A lower resistivity zone  
343 (blue area) was identified upstream within the northern portion of the riffle section (Fig. 3b, iii). The riffle portion  
344 of the river was also accompanied by a break in the high resistivity trend observed along the south shoreline. A  
345 lower average resistivity was observed during warmer low-flow conditions indicating that a portion of the response  
346 may be dependent on formation temperature (i.e.,  $5^\circ\text{C}$  to  $20^\circ\text{C}$  fluctuations). Formation resistivities varied up to 10  
347 % within the pool and up to 18 % within the riffle. While the average change in riverbed resistivity was 16 %,   
348 portions of the riverbed further down and upstream of the resistivity transects did exhibit early-spring to mid-  
349 summer fluctuations up to 30 %.

### 350 4.3 Time-Lapse Electrical Resistivity Imaging

#### 351 4.3.1 Electrical Resistivity Models

352 Figure 10 provides a summary of the inverted model results at the pool and riffle sections for the full study period.  
353 The mean inverted model resistivity and data range for each sample event is presented along with the number of  
354 apparent resistivity data points removed from the dataset prior to inversion, and the root mean squared (RMS) error  
355 of the inverted model. Although the resistivity distribution across the pool remained systematically higher than the  
356 riffle throughout the entire monitoring period, both locations exhibited a dynamic response over the annual cycle. A  
357 greater number of measurements had to be removed prior to inversion of frozen-period data sets, which may have  
358 contributed to the higher RMS errors encountered during the winter period. A subset of the inverted resistivity  
359 models over the annual cycle (i.e., samples a–h identified in Fig. 10) are shown in Fig. 11. These snapshots capture  
360 the spatiotemporal evolution of predominant geoelectrical conditions beneath the riverbed.

361 Spatial electrical resistivity data were highly variable across the pool (Fig. 11a–h). The highest resistivities were  
362 observed along the south shoreline, which coincided with the presence of competent bedrock (Fig. 3b, i), with  
363 limited vertical and horizontal fractures. Similarly resistive conditions extended southward onto the floodplain.  
364 Subsurface conditions became less resistive toward the north shoreline, which coincided with the presence of  
365 increased fractures and dissolution features, mechanically broken or weathered bedrock, and a thin layer of organic  
366 rich sediment alongside the north shoreline and floodplain. Initial surveys conducted across the pool on 25-Jul-2014  
367 identified a relatively low resistivity zone ( $<1000 \Omega \text{ m}$ ) extending 2 m beneath the riverbed that spanned the full



368 width of the river. Measurements on 26-Sep-2014 through 24-Dec-2014 captured the retraction of this zone toward  
369 the north shore. During this period the resistivity across the full transect increased only slightly. The onset of  
370 frozen ground and river conditions on 29-Jan-2014 resulted in an abrupt shift in the resistivity distribution. A high  
371 resistivity zone formed above the water table across the southern floodplain and was accompanied by an increase in  
372 resistivity across the full river profile. It is important to note that these frozen periods were accompanied by higher  
373 model RMS errors, and thus, our interpretation of these data focus on long-period trends. The formation of river ice  
374 (basal and surface ice) may have altered the true geometry of the surface water body represented in the model,  
375 potentially contributing to the higher RMS errors. The arrival of seasonal thaw conditions on 27-Mar-2015 was  
376 accompanied by reduced resistivities across the river as rock and river ice progressively thawed and was mobilized  
377 by spring freshet. Further seasonal warming on 6-May-2015 and 3-July-2015 resulted in a systematic decrease in  
378 riverbed resistivity from the north to south shoreline.

379 Riverbed resistivity across the riffle portion of the river (Fig. 11a–h) was markedly different with respect to the  
380 distribution and magnitude of resistivity fluctuations. The riffle exhibited a zone of comparatively low resistivity  
381 ( $<100 \Omega \text{ m}$ ) that extended slightly deeper than that at the pool, to a depth of 3 m. The initial survey on 26-Jul-2014  
382 identified a zone of very low resistivity that progressively became more resistive over time (26-Sep-2014 through  
383 24-Dec-2014). Much like the pool, however, this low resistivity zone reverted back toward the north shoreline. The  
384 onset of seasonally frozen river conditions was accompanied by an increase in resistivity across a significant portion  
385 of the riverbed. Inverse models during frozen water conditions were again accompanied by higher RMS errors,  
386 which we attribute to the formation of river ice which could not be accounted for in the model. Unlike the pool,  
387 which experienced the formation of a substantial zone of ground frost along the south shore, less ground frost was  
388 observed at depth along the riverbanks bounding the riffle. Spring thaw brought reduced resistivities across the  
389 riverbed with subtle lateral variations, followed by the beginnings of a less-resistive riverbed zone emanating  
390 southward from the north shoreline. The bedrock resistivity below 3 m depth remained relatively constant through  
391 the monitoring period.

#### 392 4.3.2 Spatiotemporal Resistivity Trends

393 A resistivity index (RI) was calculated using Eq. (3) to assess spatiotemporal variations in electrical resistivity  
394 within predefined zones (Fig. 5) of the bedrock beneath the river (Fig. 12); zones A and D represent conditions  
395 along the south and north riverbank, while zones B and C represent conditions within the southern and northern  
396 portions the river. These zones were defined based on their representative areas and the magnitude of the temporal  
397 fluctuations observed over the full monitoring period (Fig. 11). A RI of zero indicates a mean zone resistivity  
398 (MZR) that is equal to the mean annual resistivity (MAR) of the whole profile. An index of +1 indicates a  
399 resistivity that is twice the annual mean, while an index of -0.5 indicates a resistivity that is half the annual mean.

400 The RI time-series for the pool (Fig. 12a) and riffle (Fig. 12b) capture the magnitude and frequency of the temporal  
401 variability observed within these four representative zones. Relative to the MAR, the pool exhibited larger and more  
402 frequent fluctuations in resistivity compared to the riffle. The south shoreline (zone A) at the pool was more  
403 dynamic than the corresponding zone at the riffle; zone A at the pool encompasses a larger unsaturated zone, which



404 is more likely impacted by changes in temperature and saturation, especially during the freezing and thawing period.  
405 The north shoreline (zone D) at the pool and riffle exhibited lower than average resistivities with relatively minimal  
406 transience over the study period, with the exception of the mid-to-late-winter freeze-up. Here, a variable layer of  
407 sediment and organic matter with higher water content likely moderated freeze-thaw fluctuations relative to sections  
408 of exposed rock. Conditions below the riverbed (zones B and C) exhibited both longer-period (seasonal) and  
409 shorter-period (intra-seasonal) fluctuations. While the relative changes observed at the pool were larger than the  
410 riffle, similar seasonal trends were observed at each location. Zones B and C at the pool were mutually consistent,  
411 while those at the riffle were somewhat less consistent.

412 Although perturbations were observed in the resistivity beneath the riverbed before and after winter freeze-up (e.g.,  
413 zones B and C), the responses were significantly dampened relative to the winter period. Events 13, 26 and 31 (Fig.  
414 4 and 7), which correspond to periods of increase precipitation, may coincide with observed perturbations in the RI;  
415 however, based on these data it is not clear whether the riverbed resistivity and surface water responses are mutually  
416 consistent; this limited correlation may suggest that groundwater discharge in this section of the river is strong, and  
417 thus, limiting potential groundwater-surface water mixing, at least at the spatial scales considered in this study.  
418 Therefore, these observed geophysical dynamics within the riverbed may be associated with seasonal temperature  
419 transience with secondary effects due to solute fluctuations.

## 420 5.0 Discussion

### 421 5.1 Influence of Water Properties on Formation Resistivity

422 Riverbed electrical resistivity mapping during high and low stage conditions identified a spatiotemporal response  
423 within the upper 6 m of rock, which varied with riverbed morphology. Long-term resistivity monitoring along fixed  
424 profiles over the pool and riffle portions of the river revealed a transient zone within the upper 2 and 3 m of bedrock,  
425 respectively. In particular, the formation of a low resistivity zone (high electrical conductivity) was observed during  
426 the warmer summer period that diminished as the environment cooled. While pore water conductivity depends on  
427 electrolytic concentration and temperature, their individual contribution to the bulk formation response cannot be  
428 decoupled across the entire study area given inherent/practical limitations in the number of direct measurement  
429 points in a bedrock environment. Although this ambiguity in the driving mechanism of observed electrical changes  
430 below the riverbed hinders our ability to definitively define the vertical extent of a potential groundwater-surface  
431 water mixing zone, our geophysical data set does suggest that a groundwater-surface water mixing in a bedrock  
432 environment may be limited, in part by strong upward hydraulic gradients and groundwater discharge at this site.

433 Aqueous temperature and specific conductance measurements collected in the river stage gauge (RSG1) and shallow  
434 bedrock well (SCV6) provided end-member conditions (Fig. 7). These data were used to assess the influence of  
435 aqueous conditions on bulk formation resistivity (Fig. 8). While some degree of overlap was observed between  
436 groundwater and surface water properties, they were generally differentiable across the study area. That said,  
437 aqueous temperature fluctuations likely dominated the bulk electrical response over the full annual cycle. Given the  
438 impact of temperature on the bulk formation resistivity, observed bedrock resistivity dynamics are attributed to



439 changes in water/rock temperature with secondary effects caused by changes in electrolytic concentration. These  
440 findings are consistent with Musgrave and Binley (2011), who concluded that temperature fluctuations over an  
441 annual cycle within a temperate wetland environment with groundwater electrical conductivities ranging from 400  
442  $\mu\text{S cm}^{-1}$  to 850  $\mu\text{S cm}^{-1}$  dominated formation resistivity transience. Of course, our annual temperature range was  
443 more extreme than that of Musgrave and Binley, we examined electrical dynamics within a very different medium  
444 (rock versus organic rich sediment), and ultimately captured a broader range of seasonal conditions that included  
445 ground frost and riverbed ice formation.

446 Measurements collected with a shorter time-step (diurnal) and shorter electrode spacing may capture more transient  
447 rainfall or snowpack melt episodes, possibly leading to the identification of electrolytic-induced transients beneath  
448 the riverbed indicative of a groundwater-surface water mixing zone. Based on the short period of intraseasonal  
449 fluctuations observed in Fig. 12, and the timing and duration of major precipitation or thawing events (5 to 7 day  
450 cycles) (Fig.4), it is reasonable to assume that our geophysical time step (days to weeks) was accompanied by some  
451 degree of aliasing. Finally, it is possible that shallower sections of rock within the river exposed to direct sunlight  
452 during the day, which can vary depending on cloud cover (daily) and the sun's position in the sky (seasonally), may  
453 have exhibited a wider range, or more transient temperature fluctuations, than those areas beneath or adjacent to a  
454 canopy. A closer inspection of the unfrozen temporal response in zone B reveals a wider range in resistivity relative  
455 to the more northern zone C. At this latitude in the northern hemisphere the south shore will receive more direct  
456 sunlight; it is possible that the shallow rock on this side of the river experienced greater fluctuations in temperature  
457 (both seasonally and diurnally), thereby contributing to the observed geoelectrical dynamics.

## 458 **5.2 Formation of Ground Frost and Anchor Ice**

459 A dramatic increase in bedrock resistivity was observed with the onset of freezing ground conditions; this can  
460 impact a wide range of infrastructure (e.g., dams, hydropower generation), ecologic (e.g., alteration of fish and  
461 benthic habitats) and hydraulic functions (e.g., river storage, baseflow) (Beltaos and Burrell 2015). The formation of  
462 a highly resistivity zone consistent with a seasonal frost front within the unsaturated portion of the riverbank (Fig.  
463 11e; zone A in Fig. 12a), and the accumulation of river ice resulted in marked changes in resistivity. These winter  
464 season effects are readily evident in Fig. 12. The magnitude of the resistivity increase observed at the pool and riffle  
465 may suggest a potential reduction in the hydraulic connectivity between surface water and groundwater during the  
466 winter months.

467 Ground frost primarily formed along the riverbank over the southern floodplain at the pool. This topographically  
468 higher area was relatively devoid of large vegetation (Fig. 2), and thus, experienced more severe weather conditions  
469 (e.g., higher winds resulted in less snow pack to insulate the ground). These conditions likely enhanced the  
470 formation of a thick frost zone which propagated to the water table (pool in Fig. 11e). The adjacent northern  
471 riverbank and those up-gradient at the riffle were topographically lower (i.e., thinner unsaturated zone) and were  
472 sheltered by large trees. The formation of a seasonal frost zone along the riverbank may have implications to  
473 baseflow dynamics during the winter months and early-thaw period.



474 The presence of river ice did have a noticeable impact on the inverse model results as reflected in the higher RMS  
475 errors at the pool (>6 %) and riffle (>4 %) during the winter period (Fig. 10). This was particularly evident at the  
476 pool, which exhibited a more uniform high resistivity zone beneath the riverbed (Fig. 11e). A simple sensitivity  
477 analysis of the inversion process using different constraints on surface water geometry and aqueous electrical  
478 resistivity suggests that model convergence was highly dependent on surface water geometry and its actual  
479 resistivity. For instance, applying an aqueous resistivity of one-half the true value led to very poor model  
480 convergence and substantial overestimates of river resistivity. The riffle was relatively less sensitive to surface  
481 water properties likely because of its overall lower river stage compared to the pool, and hence, relatively lower  
482 impact of the surface water body on the apparent resistivity measurement. This sensitivity to surface water  
483 properties is a consequence of the high electrical contrast between the conductive surface water and resistive  
484 bedrock. Anchor ice further reduced the electrical connectivity across the riverbed, while the ice crust along the  
485 surface of the water altered the effective geometry of the water body, thereby impacting the inverse solution.  
486 Unfortunately, direct measurements of river ice thickness were not collected, and thus could not be explicitly  
487 incorporated into the surface water layer conceptualization during the winter months. Nevertheless, the effect of  
488 river ice on the inverse models appears to be limited to the rock immediately beneath the surface water layer.

### 489 **5.3 Implications to the Conceptualization of Groundwater-Surface Water Exchange in Bedrock Rivers**

490 The fractured dolostone in this study consists of a visible orthogonal joint network approximately orientated at 10°  
491 to 20° NNE and 280° to 290° SNW, consistent with the regional joint orientations, with frequencies ranging from  
492 centimeter to sub-meter scale where exposed at surface. Streambed resistivity measurements indicate a dynamic  
493 groundwater zone within the upper 2 m to 3 m of riverbed. A less-resistive zone (<1000 Ω m) was observed  
494 beneath the pool emanating from the north shoreline during warmer low-flow periods (July and August 2014). This  
495 zone retracted in late-summer but showed signs of reappearance in early July 2015. A similarly evolving low-  
496 resistivity zone (<100 Ω m) was observed across the riffle, but was more variable across the river transect. While  
497 dynamic fluctuations in temperature and aqueous conductivity support the potential existence of a definitive  
498 groundwater-surface water mixing zone, it is not yet clear how these geoelectrical dynamics were influenced or  
499 enhanced by fluid flow in the discrete fractures, or seasonal thermal gradients across the riverbed.

500 While groundwater-surface water exchange within a fractured bedrock river are expected, discrete fracture networks  
501 and dissolution-enhanced features will support more heterogeneous and anisotropic surface water mixing zones  
502 compared to porous unconsolidated sediment. Swanson and Cardenas (2010) examined the utility of using heat as a  
503 tracer of groundwater-surface water exchange across a pool-riffle-pool sequence. Observed thermal patterns and  
504 zones of influence (i.e., effective mixing zones) in their study were consistent with conceptual models depicting a  
505 pool-riffle-pool sequence. While similar temperature dynamics may be expected across the pool-riffle-pool  
506 sequence in a bedrock environment, our coarser temporal sampling interval (days to weeks) combined with our  
507 smoothed resistivity models limited our ability to capture subtle diel temperature transience across discrete fractures  
508 or flow features. Although the electrical resistivity method was not able to definitively resolve a groundwater-



509 surface water mixing zone, these data do provide insight into the magnitude, lateral extent and spatiotemporal scale  
510 of geoelectrical transience within the upper few meters of rock.

## 511 **6.0 Conclusions**

512 Electrical resistivity methods were used to investigate the temporal geoelectrical response beneath a bedrock river  
513 within the upper 6 meters of rock over a full annual cycle. Induced resistivity measurements across the 200 m reach  
514 of the river during high and low flow conditions showed that spatiotemporal variations were dependent upon  
515 riverbed morphology. Time-lapse electrical resistivity imaging of the pool and riffle portion of the river, sampled on  
516 a semi-daily to semi-weekly interval, showed consistently higher resistivity at the pool with more elevated  
517 resistivities along the south shoreline. The formation of a transient 2 m thick low-resistivity zone within the pool in  
518 mid-summer appears to be associated with an increase in surface water/bedrock formation temperatures during  
519 seasonally low river flux. Conversely, the riffle was characterized by a 3 m thick low-resistivity zone spanning the  
520 entire width of the river, underlain by a more resistive material. These lower resistivities at the riffle suggest the  
521 presence of more porous bedrock material consistent with enhanced-dissolution of rock and/or a layer of weathered  
522 bedrock zone overlying competent rock.

523 Although seasonal geoelectrical dynamics were observed at both the pool and riffle, the pool was more transient and  
524 exhibited a broader range, yet spatially more uniform distribution in resistivity. Conversely, the riffle exhibited more  
525 lateral variability in resistivity along across the riverbed. Seasonal cooling was accompanied by a higher-resistivity  
526 zone emanating from the south shore to north shore in both the pool and riffle. This resistivity trend reversed during  
527 the seasonal warming cycle, becoming less-resistive toward the south shoreline as seasonal temperatures increased  
528 and river flow decreased. The formation of ground frost and basal ice along the riverbed had a strong and  
529 sometimes negative impact on the seasonal resistivity profiles during the winter months. Intraseasonal geoelectrical  
530 transience associated with major precipitation events, which were accompanied by short-period perturbations in  
531 surface water temperature and specific conductance had a relatively small impact on riverbed resistivity. This may  
532 be explained by the presence of a strong groundwater discharge zone across this reach of the river, which may have  
533 limited or moderated the electrical resistivity changes within the suspected groundwater-surface water mixing zone.

534 Time-lapse temperature profiling within the angled borehole underlying the river revealed active groundwater flow  
535 zones. While our resistivity measurements captured geoelectrical dynamics within the upper few meters of riverbed,  
536 these data are indirect evidence of a groundwater surface water mixing zone; whether the observed geoelectrical  
537 transience are primarily a function of seasonal temperature fluctuations or transience in ionic concentration, in  
538 response to precipitation events, will require further investigation. Nevertheless, our study demonstrates that surface  
539 electrical resistivity has the capacity to detect and resolve changes in electrical resistivity within a bedrock riverbed.  
540 Given the complex fracture distribution, geometry and dissolution features inherent to sedimentary rock, surface  
541 resistivity methods may be most effective in the initial design and placement of more direct measurement methods,  
542 thereby reducing instrumentation costs and impacts to ecosensitive environments.



543 **DATA AVAILABILITY**

544 The data used in this study are presented in the figures. Complete monitoring data sets (Figures 10 and 11) and can  
545 be made available upon request from the corresponding author.

546

547 **TEAM LIST**

548 **Steelman, Kennedy, Capes, Parker**

549

550 **AUTHOR CONTRIBUTION**

551 **Steelman** designed the experiment, conducted the surveys, and analysed the geophysical data; **Kennedy** designed  
552 the borehole network, logged the core, instrumented the hydrological monitoring network; **Capes** designed and  
553 collected the temperature profiles, logged the core and supported hydrological data collection and interpretation;  
554 **Parker** contributed to the design of the hydrological geophysical monitoring network, and supported conceptual  
555 understanding of groundwater flow through fractured rock.

556

557 **COMPETING INTERESTS**

558 The authors declare that they have no conflict of interest.

559

560 **ACKNOWLEDGEMENTS**

561 This research was made possible through funding by the Natural Sciences and Engineering Research Council of  
562 Canada in the form of a Banting Fellowship to Dr. Steelman, and an Industrial Research Chair (Grant #  
563 IRCPJ363783-06) to Dr. Parker. The authors are very appreciative of the field contributions of staff and students at  
564 the University of Guelph and University of Waterloo, particularly field-technicians Dan Elliot and Bob Ingleton.  
565 This work would not have been possible without land-access agreements with Scouts Canada, Ontario Ministry of  
566 Natural Resources, and river-flow data provided by the Grand River Conservation Authority.

567



568 **REFERENCES**

- 569 Alexander, M. D. and Caissie, D.: Variability and comparison of hyporheic water temperatures and seepage fluxes  
570 in a small Atlantic Salmon stream, *Groundwater*, 41, 72-82, 2003.
- 571 Anderson, M. P.: Heat as a ground water tracer, *Ground Water*, 43, 951-968, 2005.
- 572 Archie, G. E.: The electrical resistivity log as an aid in determining some reservoir characteristics, *T. Am. Inst.*  
573 *Mineral. Metall. Petrol. Eng.*, 146, 54-62, 1942.
- 574 Arps, J. J.: The effect of temperature on the density and electrical resistivity of sodium chloride solutions, *Trans.*  
575 *A.I.M.E.*, 164, 54-62, 1953.
- 576 Beltaos, S. and Burrell, B. C.: Hydrotechnical advances in Canadian river ice science and engineering during the  
577 past 35 years, *Can. J. Civ. Eng.*, 42, 583-591, dx.doi.org/10.1139/cjce-2014-0540, 2015.
- 578 Bianchin, M. S., Smith, L., and Beckie, R. D.: Defining the hyporheic zone in a large tidally influenced river, *J.*  
579 *Hydrol.*, 406, 16-29, doi:10.1016/j.jhydrol.2011.05.056, 2011.
- 580 Binley, A., Ullah, S. Heathwaite, A. L., Heppell, C., Byrne, P., Lansdown, K., Trimmer, M., and Zhang, H.:  
581 Revealing the spatial variability of water fluxes at the groundwater-surface water interface, *Water Resour. Res.*, 49,  
582 3978-3992, doi:10.1002/wrcr.20214, 2013.
- 583 Boano, F., Revelli, R., and Ridolfi L.: Reduction of the hyporheic zone volume due to the stream-aquifer interaction,  
584 *Geophys. Res. Lett.*, 35, L09401, doi:10.1029/2008GL033554, 2008.
- 585 Brassington, R.: *Field Hydrogeology*, John Wiley & Sons, Inc, 1998.
- 586 Briggs, M. A., Lautz, L. K., McKenzie, J. M., Gordon, R. P., and Hare, D. K.: Using high-resolution distributed  
587 temperature sensing to quantify spatial and temporal variability in vertical hyporheic flux, *Water Resour. Res.*, 48,  
588 W02527, doi:10.1029/2011WR011227, 2012.
- 589 Brunton, F. R.: Update of revisions to the Early Silurian stratigraphy of the Niagara Escarpment: integration of  
590 sequence stratigraphy, sedimentology and hydrogeology to delineate hydrogeologic units, In *Summary of Field*  
591 *Work and Other Activities 2009*, Ontario Geologic Survey, Open File Report 6240, pp. 25-1 to 25-20, 2009.
- 592 Campbell, R. B., Bower, C. A., and Richards, L. A.: Change of electrical conductivity with temperature and the  
593 relation of osmotic pressure to electrical conductivity and ion concentration for soil extracts, *Soil Sci. Soc. Am.*  
594 *Proc.*, 12, 66-69, 1948.
- 595 Cardenas, M. B. and Markowski, M. S.: Geoelectrical imaging of hyporheic exchange and mixing of river water and  
596 groundwater in a large regulated river, *Environ. Sci. Technol.*, 45, 1407-1411, dx.doi.org/10.1021/es103438a, 2011.
- 597 Cole, J., Coniglio, M., and Gautrey, S.: The role of buried bedrock valleys on the development of karstic aquifers in  
598 flat-lying carbonate bedrock: insights from Guelph, Ontario, Canada, *Hydrogeol. J.*, 17, 1411-1425,  
599 doi:10.1007/s10040-009-0441-3, 2009.



- 600 Conant Jr., B.: Delineating and quantifying ground water discharge zones using streambed temperature,  
601 Groundwater, 42, 243-257, 2004.
- 602 Constantz, J.: Heat as a tracer to determine streambed water exchanges, Water Resour. Res., 44, W00D10, doi:  
603 10.1029/2008WR006996, 2008.
- 604 Coscia, I., Greenhalgh, S. A., Linde, N., Doetsch, J., Marescot, L., Günther, T., Vogt, T., and Green, A. G.: 3D  
605 crosshole ERT for aquifer characterization and monitoring of infiltrating river water, Geophysics, 76, G49-G59, doi:  
606 10.1190/1.3553003, 2011.
- 607 Coscia, I., Linde, N., Greenhalgh, S., Vogt, T., and Green, A.: Estimating traveltimes and groundwater flow pattern  
608 using 3D time-lapse crosshole ERT imaging of electrical resistivity fluctuations induced by infiltrating river water,  
609 Geophysics, 77(4), E239-E250, doi: 10.1190/GEO2011-0328.1, 2012.
- 610 Crook, N., Binley, A., Knight, R., Robinson, D. A., Zarnetske J., and Haggerty, R.: Electrical resistivity imaging of  
611 the architecture of substream sediments, Water Resour. Res., 44, W00D13, doi:10.1029/2008WR006968, 2008.
- 612 Crosbie, R. S., Taylor, A. R., Davis, A. C., Lamontagne, S., and Munday, T.: Evaluation of infiltration from losing-  
613 disconnected rivers using a geophysical characterisation of the riverbed and a simplified infiltration model, J.  
614 Hydrol., 508, 102-113, <http://dx.doi.org/10.1016/j.jhydrol.2013.07.045>, 2014.
- 615 Dimova, T. N., Swarzenski, P.W., Dulaiova, H., and Glenn, C. R.: Utilizing multichannel electrical resistivity  
616 methods to examine the dynamics of the fresh water-seawater interface in two Hawaiian groundwater systems, J.  
617 Geophys. Res., 117, C02012, doi: 10.1029/2011JC007509, 2012.
- 618 Doetsch, J., Linde, N., Vogt, T., Binley, A., and Green, A. G.: Imaging and quantifying salt-tracer transport in a  
619 riparian groundwater system by means of 3D ERT monitoring, Geophysics, 77, B207-B218, doi:10.1190/GEO2012-  
620 0046.1, 2012.
- 621 Doro, K. O., Leven, C., and Cirpka, O. A.: Delineating subsurface heterogeneity at a loop of River Steinlach using  
622 geophysical and hydrogeological methods, Environ. Earth Sci., 69, 335-348, doi:10.1007/s12665-013-2316-0, 2013.
- 623 Ellis, D.V.: Well logging for earth scientists, Elsevier Science Publishing Company, Inc, 1987.
- 624 Evans, E. C., Greenwood, M. T., and Petts, G. E.: Thermal profiles within river beds, Hydrol. Process., 9, 19-25,  
625 1995.
- 626 Fan, Y., Toran, L., and Schlische, R. W.: Groundwater flow and groundwater-stream interaction in fractured and  
627 dipping sedimentary rocks: insights from numerical models, Water Resour. Res., 43, W01409,  
628 doi:10.1029/2006WR004864, 2007.
- 629 Froese, D. G., Smith, D. G., and Clement, D. T.: Characterizing large river history with shallow geophysics: middle  
630 Yukon River, Yukon Territory and Alaska, Geomorphology, 67, 391-406, doi:10.1016/j.geomorph.2004.11.011,  
631 2005.



- 632 Glover, P. W. J.: A generalized Archie's law for n phases, *Geophysics*, 75, E247-E265, doi: 10.1190/1.3509781,  
633 2010.
- 634 Gourry, J.-C., Vermeersch, F., Garcin, M., and Giot, D.: Contribution of geophysics to the study of alluvial deposits:  
635 a case study in the Val d'Avaray area of the River Loire, France, *J. Appl. Geophys.*, 54, 35-49, doi:  
636 10.1016/j.jappgeo.2003.07.002, 2003.
- 637 Harrington, G. A., Gardner, W. P., and Munday, T. J.: Tracking groundwater discharge to a large river using tracers  
638 and geophysics, *Groundwater*, 52, 837-852, doi:10.1111/gwat.12124, 2014.
- 639 Hatch, C. E., Fisher, A. T., Revenaugh, J. S., Constantz, J., and Ruehl, C.: Quantifying surface water-groundwater  
640 interactions using time series analysis of streambed thermal records: Method development, *Water Resour. Res.*, 42,  
641 W10410, doi:10.1029/2005WR004787, 2016.
- 642 Irvine, D. J., Briggs, M. A., Lautz, L. K., Gordon, R. P., McKenzie, J. M., and Cartwright, I.: Using diurnal  
643 temperature signals to infer vertical groundwater-surface water exchange, *Groundwater*, version of record online 3-  
644 Oct-2016, doi: 10.1111/gwat.12459, 2016.
- 645 Johnson, T. C., Slater, L. D., Ntarlagiannis, D., Day-Lewis, F. D., and Elwaseif, M.: Monitoring groundwater-  
646 surface water interaction using time-series and time-frequency analysis of transient three-dimensional electrical  
647 resistivity changes, *Water Resour. Res.*, 48, W07506, doi:10.1029/2012WR011893, 2012.
- 648 Käser, D. H., Binley, A., and Heathwaite, A. L.: On the importance of considering channel microforms in  
649 groundwater models of hyporheic exchange, *River Res. Applic.*, 29, 528-535, doi:10.1002/rra.1618, 2013.
- 650 Keery, J., Binley, A., Crook, N., and Smith, J. W. N.: Temporal and spatial variability of groundwater-surface water  
651 fluxes: Development and application of an analytical method using temperature time series, *J. Hydrol.*, 336, 1-16,  
652 doi:10.1016/j.jhydrol.2006.12.003, 2007.
- 653 Keller, G. V.: Section V: Electrical properties, In Carmichael, R.S., ed., *CRC Practical handbook of physical*  
654 *properties of rock and minerals*, CRC Press, 361-427, 1989.
- 655 Keller, C., Cherry, J. A., and Parker, B. L.: New method for continuous transmissivity profiling in fractured rock,  
656 *Groundwater*, 52, 352-367, doi:10.1111/gwat.12064, 2014.
- 657 Knight, R. J. and Endres, A. L.: Chapter 3: An Introduction to Rock Physics Principles for Near-Surface  
658 Geophysics, In Butler, D.K., ed., *Near-Surface Geophysics*, Society of Exploration Geophysics, Tulsa, Oklahoma,  
659 31-70, 2005.
- 660 Kunert, M., Coniglio, M., and Jowett, E. C.: Controls and age of cavernous porosity in Middle Silurian dolomite,  
661 southern Ontario, *Can. J. Earth Sci.*, 35, 1044-1053, 1998.
- 662 Kunert, M. and Coniglio, M.: Origin of vertical shafts in bedrock along the Eramosa River valley near Guelph,  
663 southern Ontario, *Can. J. Earth Sci.*, 39, 43-52, doi:10.1139/E01-053, 2002.



- 664 Lemieux, J.-M., Kirkwood, D., and Therrien, R.: Fracture network analysis of the St-Eustache quarry, Quebec,  
665 Canada, for groundwater resources management, *Can. Geotech. J.*, 46, 828-841, 2009.
- 666 Loke, M. H. and Dahlin, T.: A comparison of the Gauss-Newton and quasi-Newton methods in resistivity imaging  
667 inversion, *J. Appl. Geophys.*, 49, 149-162, 2002.
- 668 Loke, M. H., Chambers, J. E., Rucker, D. F., Kuras, O., and Wilkinson, P. B.: Recent developments in the direct-  
669 current geoelectrical imaging method, *J. Appl. Geophys.*, 95, 135-156,  
670 <http://dx.doi.org/10.1016/j.jappgeo.2013.02.017>, 2013.
- 671 McLaren, R. G., Sudicky, E. A., Park, Y.-J., and Illman, W. A.: Numerical simulation of DNAPL emissions and  
672 remediation in a fractured dolomitic aquifer, *J. Contam. Hydrol.*, 136-137, 56-71,  
673 doi:10.1016/j.jconhyd.2012.05.002, 2012.
- 674 McNeill, J. D.: Electromagnetic terrain conductivity measurement at low induction numbers, Geonics Ltd. Technical  
675 Note, TN-6, 1980.
- 676 Meyer, J. R., Parker, B. L., and Cherry, J. A.: Detailed hydraulic head profiles as essential data for defining  
677 hydrogeologic units in layered fractured sedimentary rock, *Environ. Geol.*, 56, 27-44, doi:10.1007/s00254-007-  
678 1137-4, 2008.
- 679 Meyerhoff, S. B., Karaoulis, M., Fiebig, F., Maxwell, R. M., Revil, A., Martin, J. B., and Graham, W. D.:  
680 Visualization of conduit-matrix conductivity differences in a karst aquifer using time-lapse electrical resistivity,  
681 *Geophys. Res. Lett.*, 39, L24401, doi:10.1029/2012GL053933, 2012.
- 682 Meyerhoff, S. B., Maxwell, R. M., Revil, A., Martin, J. B., Karaoulis, M., and Graham, W. D.: Characterization of  
683 groundwater and surface water mixing in a semiconfined karst aquifer using time-lapse electrical resistivity  
684 tomography, *Water Resour. Res.*, 50, doi:10.1002/2013WR013991, 2014.
- 685 Miller, C. R., Routh, P. S., Brosten, T. R., and McNamara, J. P.: Application of time-lapse ERT imaging to  
686 watershed characterization, *Geophysics*, 73, G7-G17, doi: 10.1190/1.2907156, 2008.
- 687 Musgrave, H. and Binley, A.: Revealing the temporal dynamics of subsurface temperature in a wetland using time-  
688 lapse geophysics, *J. Hydrol.*, 396, 258-266, doi: 10.1016/j.jhydrol.2010.11.008, 2011.
- 689 Naegeli, M. W., Huguenberger, P., and Uehlinger, U.: Ground penetrating radar for assessing sediment structures in  
690 the hyporheic zone of a prealpine river, *J.N. Am. Benthol. Soc.*, 15, 353-366, 1996.
- 691 Norman, F. A. and Cardenas, M. B.: Heat transport in hyporheic zones due to bedforms: An experimental study,  
692 *Water Resour. Res.*, 50, 3568-3582, doi:10.1002/2013WR014673, 2014.
- 693 Novakowski, K. S. and Lapcevic, P. A.: Regional hydrogeology of the Silurian and Ordovician sedimentary rock  
694 underlying Niagara Falls, Ontario, Canada, *J. Hydrol.*, 104, 211-236, 1998.



- 695 Nyquist, J., Freyer, P. A., and Toran, L.: Stream bottom resistivity tomography to map ground water discharge,  
696 Ground Water, 46, 561-569, doi:10.1111/j.1745-6584.2008.00432.x, 2008.
- 697 Orlando, L.: Some consideration on electrical resistivity imaging for characterization of waterbed sediments, J.  
698 Appl. Geophys., 95, 77-89, doi:10.1016/j.jappgeo.2013.05.005, 2013.
- 699 Oxtobee, J. P. A. and Novakowski, K.: A field investigation of groundwater/surface water interaction in a fractured  
700 bedrock environment, J. Hydrol., 269, 169-193, 2002.
- 701 Oxtobee, J. P. A. and Novakowski, K. S.: Ground water/surface water interaction in a fractured rock aquifer,  
702 Groundwater, 41(5), 667-681, 2003.
- 703 Pehme, P. E., Parker, B. L., Cherry, J. A., and Greenhouse, J. P.: Improved resolution of ambient flow through  
704 fractured rock with temperature logs, Groundwater, 48, 191-205, doi:10.1111/j.1745-6584.2009.00639.x, 2010.
- 705 Pehme, P. E., Parker, B. L., Cherry, J. A., and Blohm, D.: Detailed measurement of the magnitude and orientation of  
706 thermal gradients in lined corehole/coreholes for characterizing groundwater flow in fractured rock, J. Hydrol., 513,  
707 101-114, <http://dx.doi.org/10.1016/j.jhydrol.2014.03.015>, 2014.
- 708 Perrin, J., Parker, B. L., and Cherry, J. A.: Assessing the flow regime in a contaminated fractured and karstic  
709 dolostone aquifer supplying municipal water, J. Hydrol., 400, 396-410, doi:10.1016/j.jhydrol.2011.01.055, 2011.
- 710 Reynolds, J.M.: An Introduction to Applied and Environmental Geophysics (2<sup>nd</sup> edition), John Wiley & Sons, 2011.
- 711 Rhoades, J. D., Raats, P. A. C., and Prather, R. J.: Effect of liquid-phase electrical conductivity, water content, and  
712 surface conductivity on bulk soil electrical conductivity, Soil Sci. Soci. Am. J., 40, 651-655, 1976.
- 713 Rucker, D. F., Noonan, G. E., and Greenwood, W. J.: Electrical resistivity in support of geological mapping along  
714 the Panama Canal, Eng. Geol., 117, 121-133, 2011.
- 715 Sambuelli, L., Leggieri, S., Calzoni, C., and Porporato, C.: Study of riverine deposits using electromagnetic methods  
716 at a low induction number, Geophysics, 72(5), B113-B120, doi:10.1190/1.2754249, 2007.
- 717 Schmidt, C., Conant Jr., B., Bayer-Raich, M., and Schirmer, M.: Evaluation and field-scale application of an  
718 analytical method to quantify groundwater discharge using mapped streambed temperatures, J. Hydrol., 347, 292-  
719 307, doi:10.1016/j.jhydrol.2007.08.022, 2007.
- 720 Silliman, S. E. and Booth, D. F.: Analysis of time-series measurements of sediment temperature for identification of  
721 gaining vs. losing portions of Juday Creek, Indiana, J. Hydrol., 146, 131-148, 1993.
- 722 Singha, K., Day-Lewis, F. D., Johnson, T., and Slater, L. D.: Advances in interpretation of subsurface processes  
723 with time-lapse electrical imaging, Hydrol. Process., 29, 1549-1576, doi:10.1002/hyp.10280, 2015.
- 724 Singha, K., Pidlisecky, A., Day-Lewis, F. D., and Gooseff, M. N. Electrical characterization of non-Fickian  
725 transport in groundwater and hyporheic systems, Water Resour. Res., 44, W00D07, doi:10.1029/2008WR007048,  
726 2008.



- 727 Sirieix, C., Riss, J., Rey, F., Prétou, F., and Lastennet, R.: Electrical resistivity tomography to characterize a karstic  
728 Vauclusean spring: Fontaine d'Orbe (Pyrénées, France), *Hydrogeol. J.*, 22, 911-924, doi:10.1007/s10040-013-1095-  
729 8, 2014.
- 730 Slater, L. D., Ntarlagiannis D., Day-Lewis, F. D., Mwakanyamale, K., Versteeg, R. J., Ward, A., Strickland, C.,  
731 Johnson, C. D., and Lane Jr. J. W.: Use of electrical imaging and distributed temperature sensing method to  
732 characterize surface water-groundwater exchange regulating uranium transport at the Hanford 300 Area,  
733 Washington, *Water Resour. Res.*, 46, W10533, doi:10.1029/2010WR009110, 2010.
- 734 Snieder, R. and Trampert, J.: Inverse problems in geophysics, In Wirgin A. (ed), *Wavefield Inversion*, Springer-  
735 Verlag, New York, pp 119-190, 1999.
- 736 Stickler, M. and Alfredsen, K. T.: Anchor ice formation in streams: a field study, *Hydrol. Process.*, 23, 2307-2315,  
737 doi:10.1002/hyp.7349, 2009.
- 738 Steelman, C. M., Kennedy, C. S., and Parker, B. L.: Geophysical conceptualization of a fractured sedimentary  
739 bedrock riverbed using ground-penetrating radar and induced electrical conductivity, *J. Hydrol.*, 521, 433-446,  
740 <http://dx.doi.org/10.1016/j.jhydrol.2014.12.001>, 2015a.
- 741 Steelman, C. M., Parker, B. L., and Kennedy, C. S.: Evaluating local-scale anisotropy and heterogeneity along a  
742 fractured sedimentary bedrock river using EM azimuthal resistivity and ground-penetrating radar, *J. Appl. Geophys.*,  
743 116, 156-166, <http://dx.doi.org/10.1016/j.jappgeo.2015.03.003>, 2015b.
- 744 Swanson, T. E. and Cardenas, M. B.: Diel heat transport within the hyporheic zone of a pool-riffle-pool sequence of  
745 a losing stream and evaluation of models for fluid flux estimation using heat, *Limnol. Oceanogr.*, 55, 1741-1754,  
746 doi: 10.4319/lo.2010.55.4.1741, 2010.
- 747 Tinkler, K.J. and Wohl E.E.: *Rivers over rock: fluvial processes in bedrock channels*. Geophysical Monograph 17,  
748 American Geophysical Union, Washington, D.C, 1998.
- 749 Toran, L., Nyquist J. E., Fang, A. C., Ryan, R. J., and Rosenberry, D. O.: Observing lingering hyporheic storage  
750 using electrical resistivity: variations around stream restoration structures, Crabby Creek, PA, *Hydrol. Process.* 27,  
751 1411-1425, doi: 10.1002/hyp.9269, 2013a.
- 752 Toran, L., Hughes, B. Nyquist, J. and Ryan, R.: Freeze core sampling to validate time-lapse resistivity monitoring of  
753 the hyporheic zone, *Groundwater*, 51, 635-640, doi: 10.1111/j.1745-6584.2012.01002.x, 2013b.
- 754 Wallin, E. L., Johnson, T. C., Greenwood, W. J., and Zachara, J. M.: Imaging high stage river-water intrusion into a  
755 contaminated aquifer along a major river corridor using 2-D time-lapse surface electrical resistivity tomography,  
756 *Water Resour. Res.*, 49, 1693-1708, doi: 10.1002/wrcr.20119, 2013.
- 757 Ward, A. S., Gooseff, M. N., and Singha, K.: Imaging hyporheic zone solute transport using electrical resistivity,  
758 *Hydrol. Process.*, 24, 948-953, doi: 10.1002/hyp.7672, 2010a



- 759 Ward, A. S., Gooseff, M. N., and Singha, K.: Characterizing hyporheic transport processes – interpretation of  
760 electrical geophysical data in coupled stream-hyporheic zone systems during solute tracer studies, *Adv. Water*  
761 *Resour.*, 33, 1320-1330, doi: 10.1016/j.advwatres.2010.05.008, 2010b.
- 762 Ward, A. S., Fitzgerald, M., Gooseff, M. N., Voltz, T. J., Binley, A. M., and Singha, K.: Hydrologic and geomorphic  
763 controls on hyporheic exchange during base flow recession in a headwater mountain stream, *Water Resour. Res.*, 48,  
764 W04513, doi: 10.1029/2011WR011461, 2012.
- 765 Waxman, M. H. and Smits, L. J. M.: Electrical conductivities in oil-bearing shaly sands, *Soc. Petrol. Eng. J.*, 8, 107-  
766 122, 1968.
- 767 White, D. S., Elzinga, C. H., and Hendricks, S. P.: Temperature patterns within the hyporheic zone of a northern  
768 Michigan river, *J. N. Am. Benthol. Soc.*, 6(2), 85-91, 1987.
- 769 Woessner, W. W.: Stream and fluvial plain ground water interactions: rescaling hydrogeologic thought,  
770 *Groundwater*, 38(3), 423-429, 2000.
- 771 Worthington, P. F.: The uses and abuses of the Archie equations, 1: The formation fracture-porosity relationship, *J.*  
772 *Appl. Geophys.* 30, 215-228, 1993
- 773 Zanini, L., Novakowski, K. S., Lapcevic, P., Bickerton, G. S., Voralek, J., and Talbot, C.: Ground water flow in a  
774 fractured carbonate aquifer inferred from combined hydrogeological and geochemical measurements, *Groundwater*,  
775 38(3), 350-360, 2000.
- 776



777

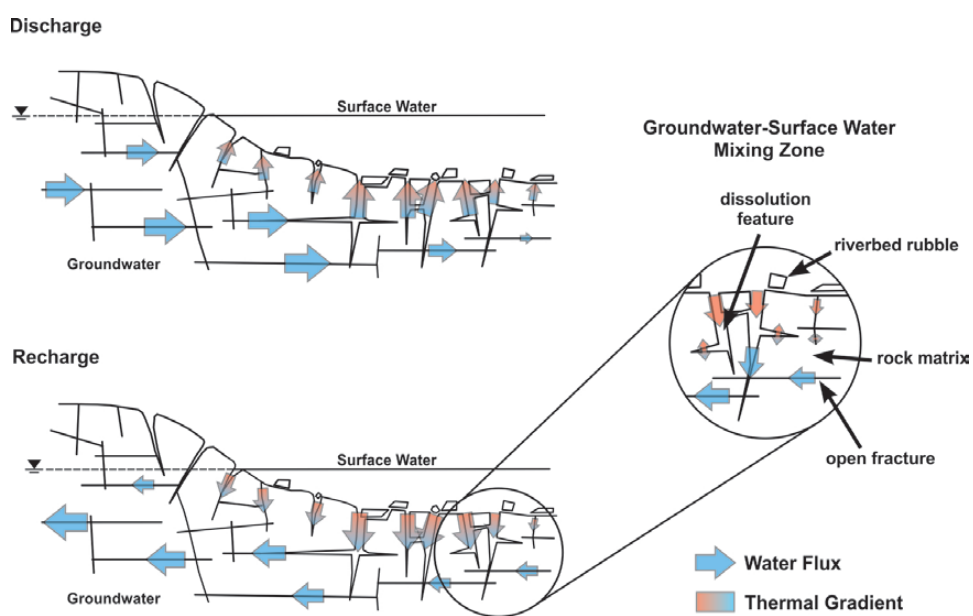
### Figures

778

779

780

781



782

783 Figure 1: General conceptual model of the groundwater flow system beneath a fractured bedrock river.

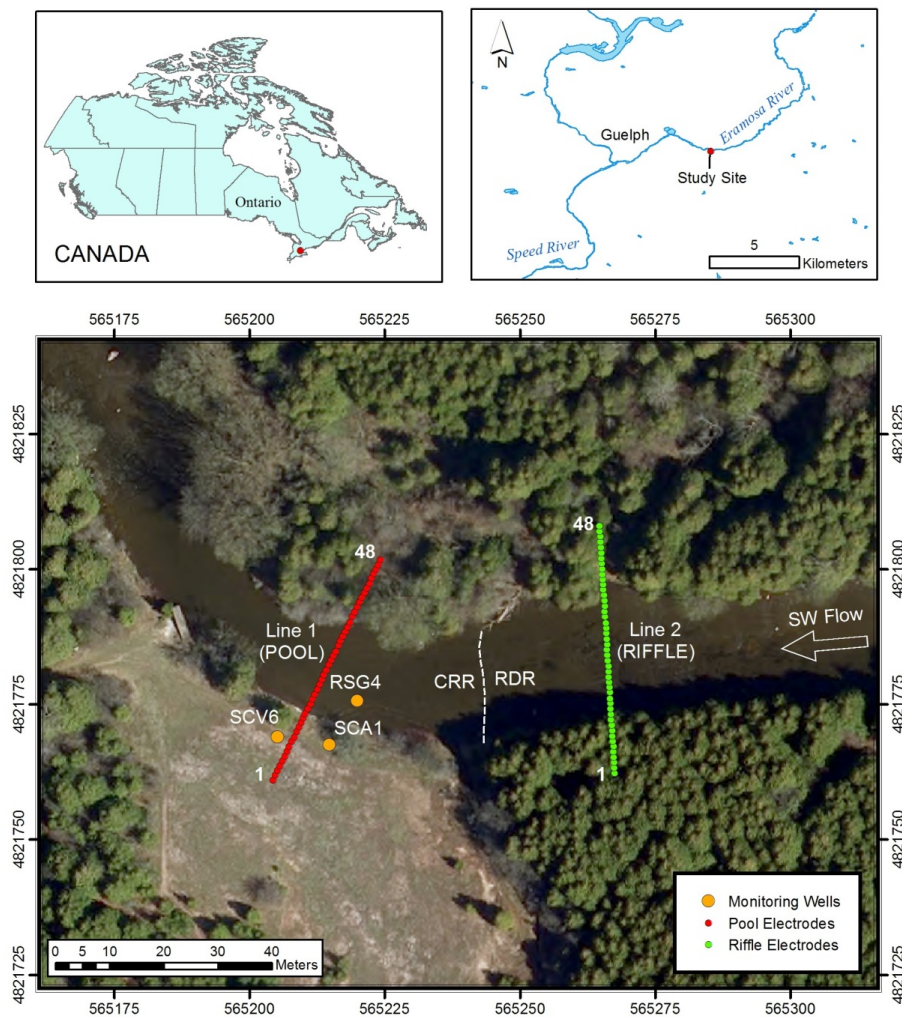
784 Groundwater-surface water mixing is controlled by open fractures and dissolution-enhanced features with secondary  
785 exchanges (flux or diffusion) occurring between fractures and rock matrix.

786



787

788



789

790 Figure 2: Field site located along the Eramosa River near Guelph, Ontario, Canada. Corehole and monitoring points  
791 are shown with fixed electrical resistivity transects located over a pool and riffle. The riverbed is described as either  
792 rubble dominated riverbed (RDR) or competent rock riverbed (CRR) surface.

793



794

795

796

797

798



799

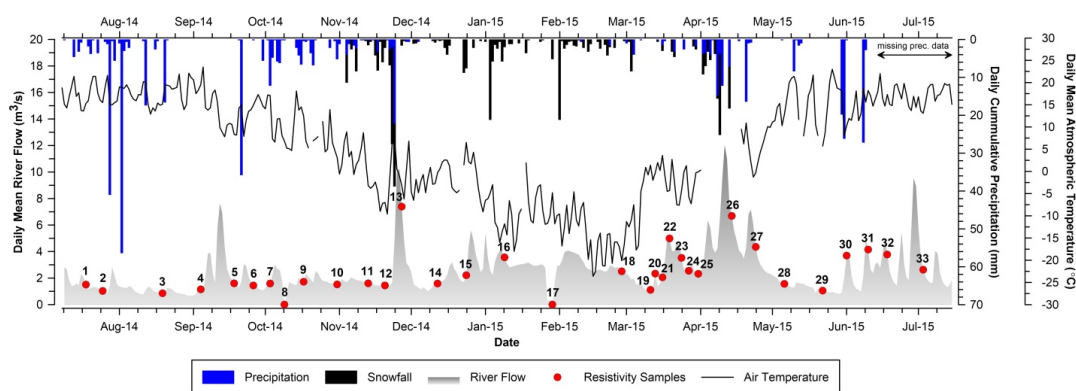
800 Figure 3: (a) Images of the river during monitored study period. (b) Examples of vertical and horizontal fracturing

801 within pool and rubble covered portions of the riverbed bedrock.

802



803  
804  
805  
806  
807  
808



809  
810  
811  
812

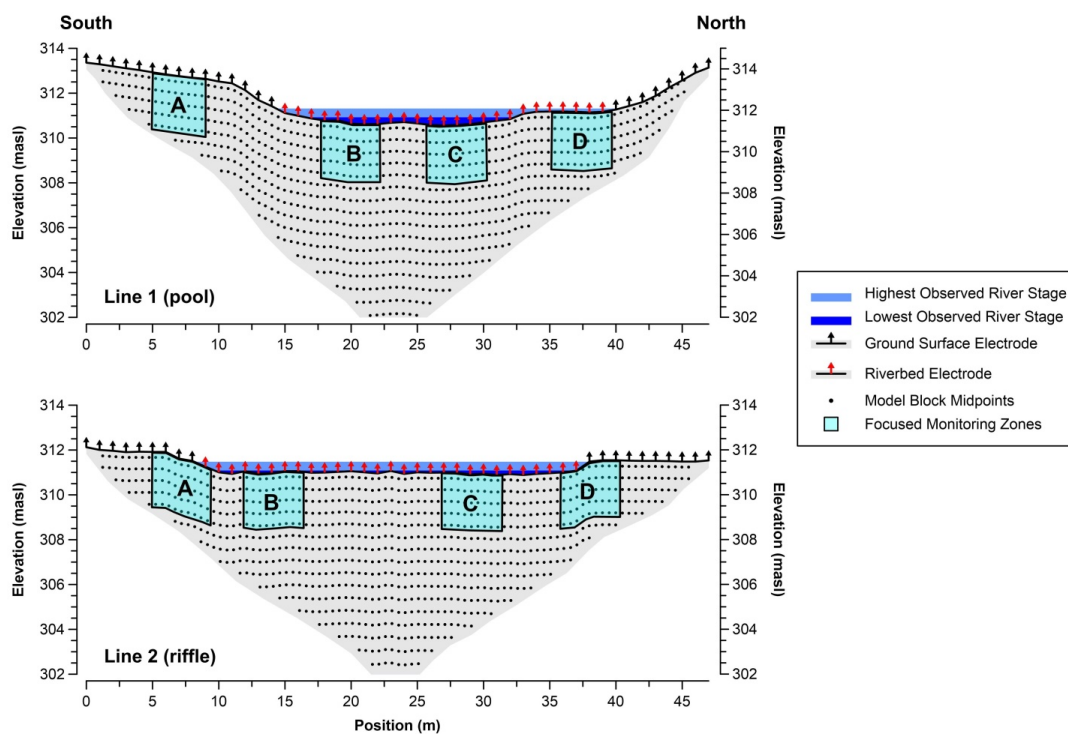
Figure 4: Continuously monitored atmospheric conditions and river flux from Watson Gauge during the study period with discrete geophysical measurement events between 18-Jul-2014 and 3-Jul-2015.



813

814

815



816

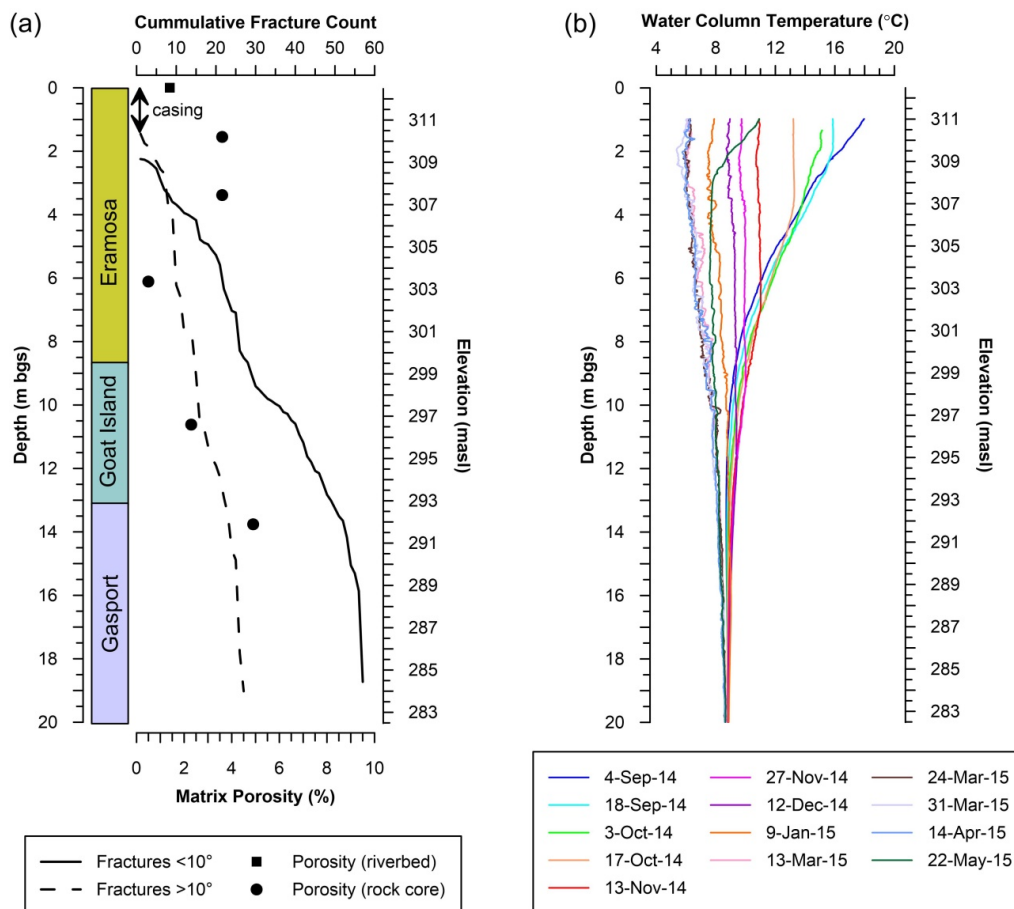
817 Figure 5: Electrical resistivity model set-up for the pool and riffle incorporating topographic variations, submerged  
818 electrodes, river stage and surface water resistivity variations. Model block points correspond to the interpreted  
819 portion of the bedrock beneath the river. Zones A, B, C and D represent areas of focused monitoring beneath the  
820 riverbed interface.

821



822

823



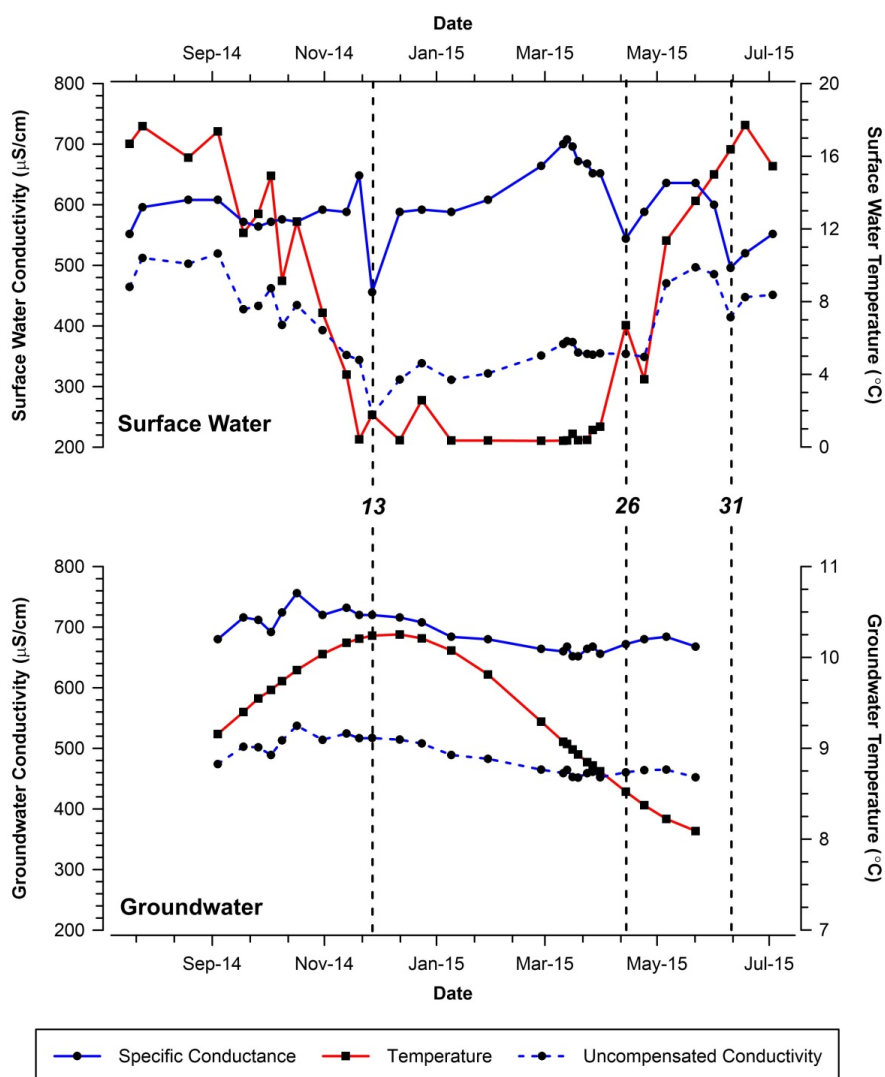
824

825 Figure 6: (a) Interpreted rock core from SCA1 (angled corehole plunging at  $60^\circ$  with an azimuth of  $340^\circ$ ). Fracture  
 826 frequency and orientations were obtained using an acoustic televiewer log, while matrix porosity measurements  
 827 were obtained from subsamples of the continuous core. (b) Corehole temperature profiles of the SCA1 Flute™  
 828 sealed water column.

829



830



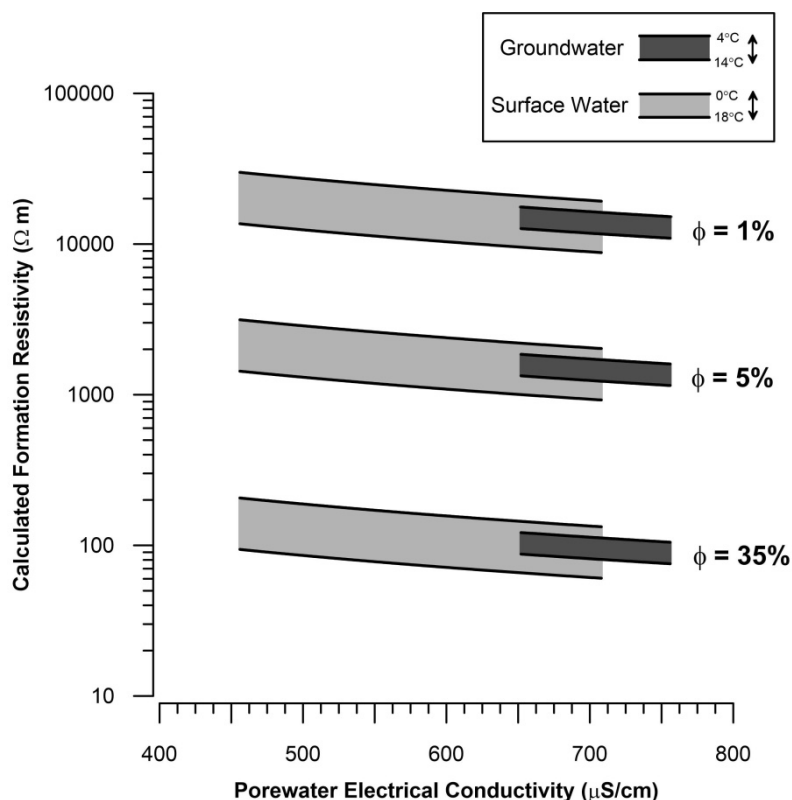
831

832 Figure 7: Specific conductance, temperature and uncompensated aqueous conductivity of surface water at RSG4 and  
 833 groundwater at the bottom of SCV6 (10.5 m bgs). Uncompensated conductivity represents the actual conductivity  
 834 of the porewater after re-incorporating the effect of temperature using the sensors internal temperature-conductivity  
 835 correction factor.

836



837  
838  
839



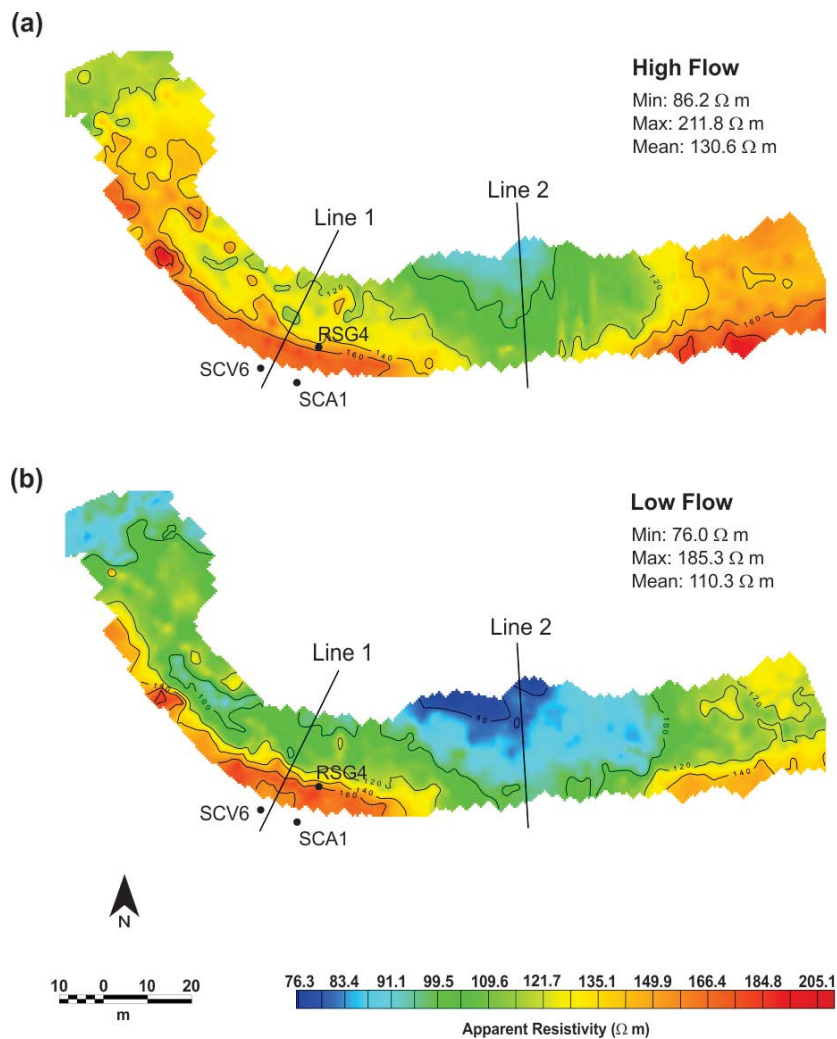
840  
841  
842  
843  
844  
845  
846  
847  
848  
849

Figure 8: Calculated formation resistivity based on Eq. (1) and measured variations in surface water and groundwater electrical conductivity including potential temperature effects based on Eq. (2). A cementation factor of 1.4 was used to represent the fractured dolostone bedrock. Measured water conductivity and temperature were obtained from CTD-Diver™ sensors deployed in RSG4 (surface water) and SCV6 (groundwater at a depth of 8 m bgs), and the continuous RBR™ temperature profiles shown in Fig. 6b. These data show the potential range in formation resistivity based on the measured range in specific conductance and temperature for three different porosity values. Porosities of 1 % and 5 % correspond to the range measured in the core, while a value of 35 % would be representative of a rubble zone.



850

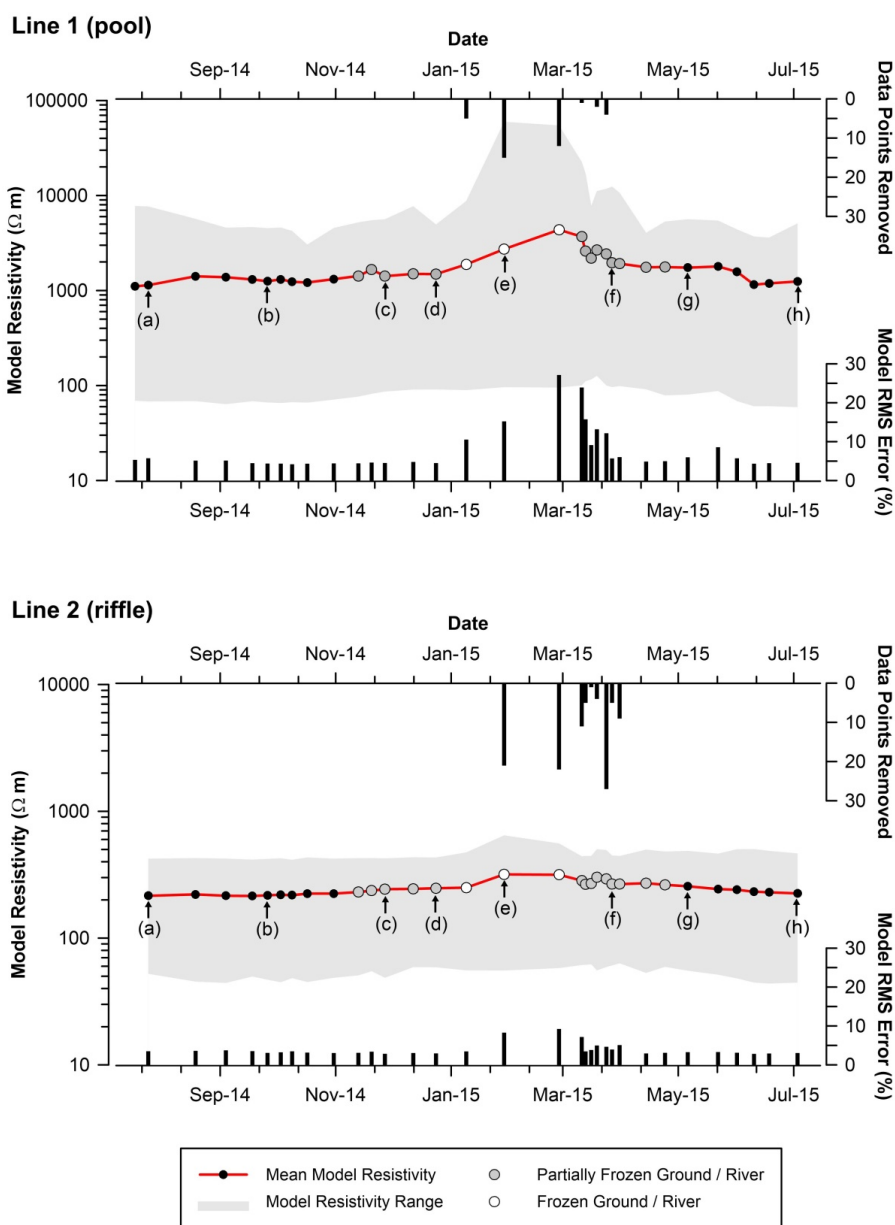
851



852

853 Figure 9: Riverbed resistivity obtained using an EM-31 ground conductivity meter during (a) high-flow/high-stage  
854 conditions on 3-Apr-2013 and (b) low-flow/low-stage conditions on 7-Jul-2014.

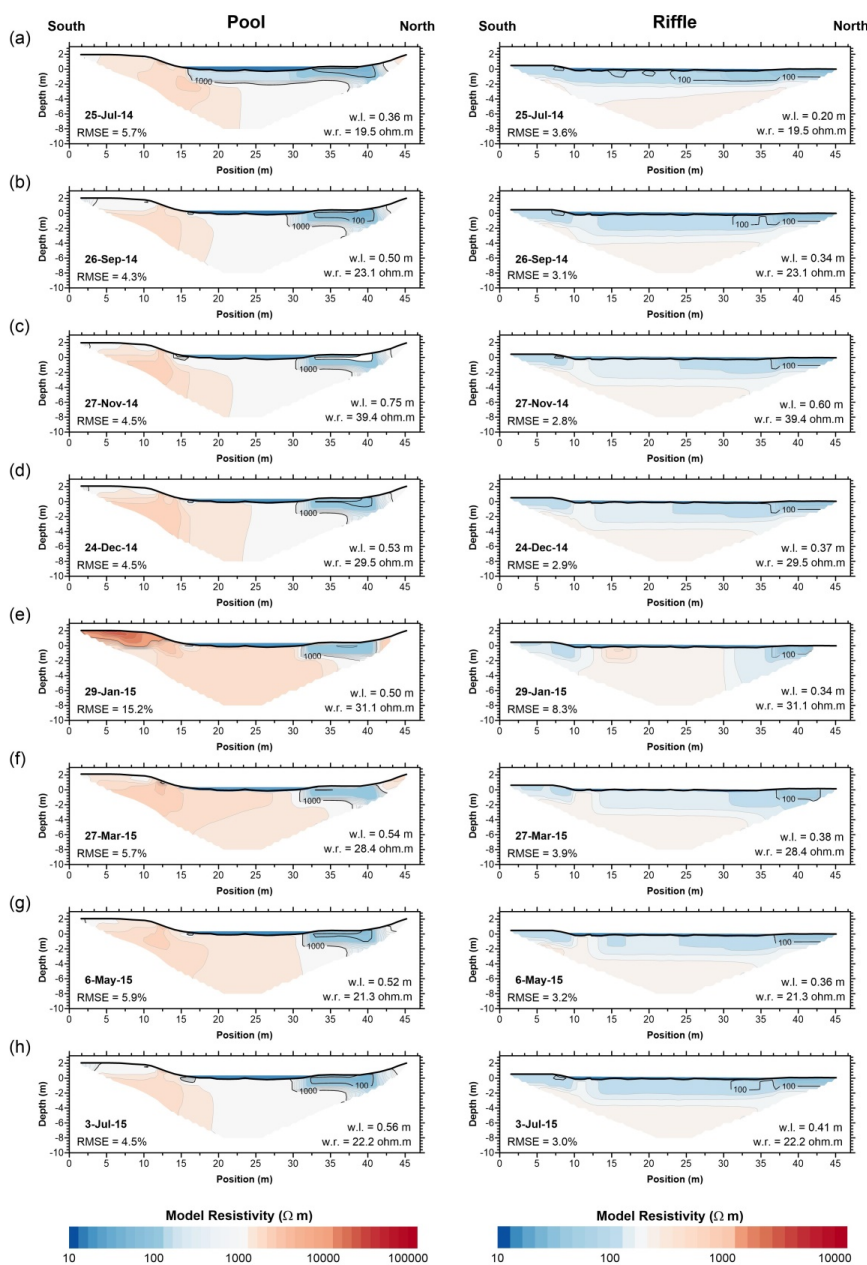
855



856

857 Figure 10: Temporal variations in inverted resistivity models for pool and riffle. Black dots represent unfrozen  
 858 conditions, grey dots indicate partially frozen conditions, while white dots indicate completely frozen river conditions.  
 859 Select resistivity models (a-h) along the time series are shown in Fig. 11.

860



861

862 Figure 11: Representative inverse resistivity models across the pool and riffle orientated from south to north.  
 863 Datasets (a-h) are identified in Fig. 10. River stage (w.l.) and surface water resistivity (w.r.) values were fixed in the  
 864 inverse model. A marked increase in resistivity was observed beneath the river during colder seasonal conditions  
 865 (November through March), while lower resistivities were observed during warmer seasonal conditions (July).

866

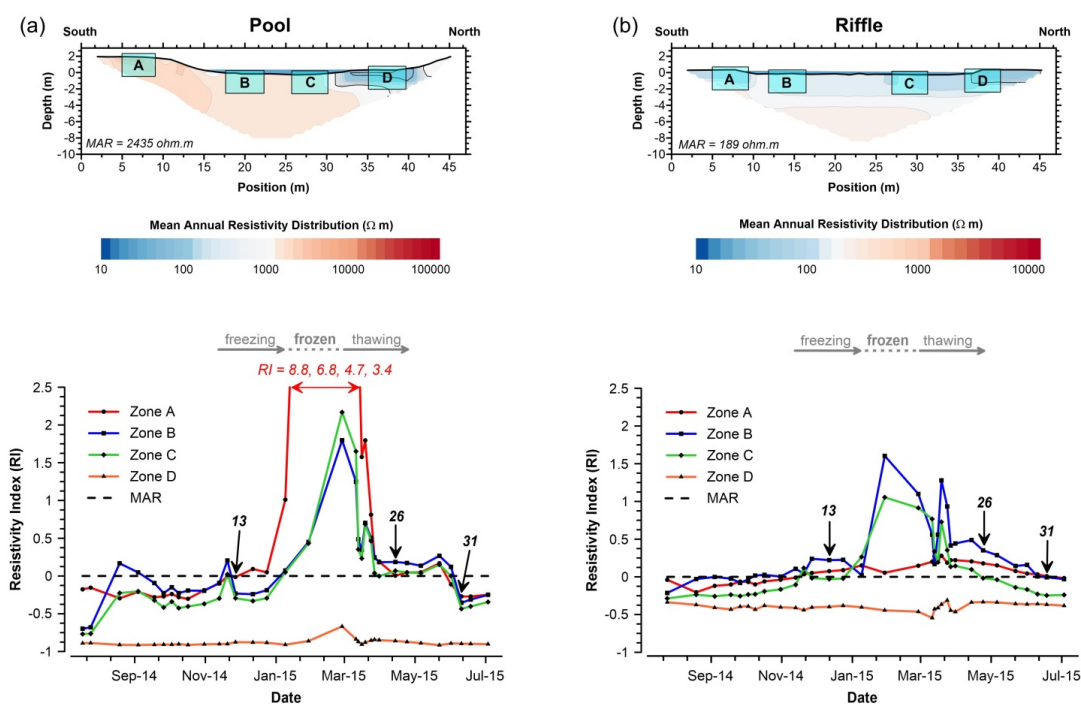


867

868

869

870



871

872 Figure 12: Spatiotemporal fluctuations in resistivity within the focused monitoring zones A, B, C and D. The  
 873 resistivity index (RI) was calculated using Eq. (3), using the mean zone resistivity (MZR) for a given measurement  
 874 date and the mean annual resistivity (MAR) of the whole profile.